Ore Geology Reviews 154 (2023) 105335

Contents lists available at ScienceDirect

Ore Geology Reviews

journal homepage: www.elsevier.com/locate/oregeorev

Palladium, platinum, selenium and tellurium enrichment in the Jiguanzui-Taohuazui Cu-Au Deposit, Edong Ore District: Distribution and comparison with Cu-Mo deposits

Xinhao Li [a,b], Guiqing Xie [a,b,*], Sarah A. Gleeson [c,d], Jingwen Mao [a,b], Zhenchao Ye [a], Yilun Jin [a]

[a] School of Earth Sciences and Resources, China University of Geosciences, Beijing 100083, China
[b] MNR Key Laboratory for Exploration Theory & Technology of Critical Mineral Resources, China University of Geosciences, Beijing 100083, China
[c] GFZ German Research Centre for Geosciences, Telegrafenberg, Potsdam 14473, Germany
[d] Institute of Geological Sciences, Freie Universität Berlin, Berlin 12249 Germany

ARTICLE INFO

Keywords:
The Jiguanzui-Taohuazui deposit
Cu-Au porphyry-skarn deposit
PGE enrichment
Selenium and tellurium

ABSTRACT

The Jiguanzui-Taohuazui Cu-Au deposit is located in the Edong ore district, Middle–Lower Yangtze River metallogenic belt, eastern China. The deposit is palladium, platinum, selenium and tellurium enriched; however, the distribution of these metals is unclear. Three mineral assemblages of ore in the deposit have been identified, namely: a magnetite-bornite-chalcopyrite-(hematite) assemblage (Mt-Bn-Cp-Hm), a chalcopyrite-pyrite assemblage (Cp-Py), and a pyrite-chalcopyrite-(sphalerite) assemblage (Py-Cp-Sph). Forty-eight bulk ore assay results show high concentrations of up to 66.9 ppb for Pd, 5.9 ppb for Pt, 150 ppm for Se and 249 ppm for Te. The high temperature Mt-Bn-Cp-Hm assemblage (530–380 °C) is enriched in Pt and Pd, whereas the Py-Cp-Sph assemblage in the marble-replacement ore (300–220 °C) hosts the major Se and Te mineralization. Palladium, Pt, and Se are mostly hosted in sulfide minerals, whereas Te is hosted in tellurides and Bi-Te-S sulfosalt minerals. Building on previous experimental and thermodynamic calculations, we propose the major controls on the Pd and Pt distribution in the deposit are temperature and salinity, whereas the Se and Te mineralization is promoted by the precipitation of major sulfide phases such as pyrite, chalcopyrite and sphalerite.

A comparison of the ores from the Jiguanzui-Taohuazui Cu-Au and Tongshankou Cu-Mo deposits in the Edong ore district shows that the Cu-Au deposit has higher PGE and Te, but similar Se concentrations. This scenario is consistent with the average grades and bulk ore contents of these elements from global (oxidized) porphyry (±skarn) Cu deposits. This suggests that the saturation of magmatic sulfides in the magma chamber as a result of higher proportion of crustal S-rich and/or reduced material contamination can be detrimental for PGE and Te enrichment processes, and thus, Cu-Au porphyry (±skarn) deposits have more potential for higher Pd and Te concentrations than the Cu-Mo deposits.

1. Introduction

Palladium, Pt, Se and Te are critical metals which can be produced as by-products of porphyry (±skarn) Cu deposits (John and Taylor, 2016). They are siderophile and chalcophile elements and tend to be enriched in the Earth's core and mantle; the average continental crust abundances of these elements are very low and have been estimated to be 1.5 ppb for Pt, 1.5 ppb for Pd, 130 ppb for Se and 1 ppb for Te (Rudnick and Gao, 2003; Lide, 2003). Palladium and Pt, as members of the platinum-group elements (PGE), prefer to bond with Fe, Ni, Cu and S, and therefore, can be enriched in metallic phases (Gunn, 2014). In the periodic table Se and Te belong to the group 16 elements, and have variable oxidation states. Overall, the chemistry of Se greatly resembles that of sulfur, hence its extensive substitution into sulfide minerals (Maslennikov et al., 2009; Keith et al., 2018). Tellurium, on the other hand, sits on the border between metals and non-metals, and its significant metallic properties and larger covalent radii (1.38 Å) result in different geochemical behavior to S and Se (Grundler et al., 2013; Keith et al., 2018; Martin et al., 2019). The major production of PGE globally comes from orthomagmatic sulfide deposits hosted in mafic and ultramafic rocks,

* Corresponding author at: MNR Key Laboratory for Exploration Theory & Technology of Critical Mineral Resources, China University of Geosciences, Beijing 100083, China.
E-mail address: xieguiqing@cugb.edu.cn (G. Xie).

https://doi.org/10.1016/j.oregeorev.2023.105335
Received 14 May 2022; Received in revised form 27 January 2023; Accepted 31 January 2023
Available online 2 February 2023

although high Pd and Pt contents have also been reported in porphyry ± skarn Cu deposits, suggesting there is some potential they could be recovered as by-products of Au and Ag production (Tarkian et al., 1991; Tarkian and Stribrny, 1999; Eliopoulos et al., 2014). Extremely high contents of Se and Te are reported in some epithermal Au-Ag deposits (Simon et al., 1997; Kouzmanov et al., 2010; Kelley and Spry, 2016; Zhai et al., 2018; Voudouris et al., 2022) and some VMS deposits (e.g., Apliki; Martin et al., 2018), however, almost all global Se and Te production comes from porphyry (±skarn) Cu deposits because of refining issues (John and Taylor, 2016). The rarity of these metals and the importance of their industrial applications means they have been classified as "critical metals" by several governments (Gunn, 2014; Schulz et al., 2017; Jowitt et al., 2018), yet few studies have reported the distribution of Se and Te in porphyry (±skarn) Cu deposits (e.g., McFall et al., 2021).

The Edong ore district, on the western margin of Middle–Lower Yangtze River metallogenic belt, is characterized by late Mesozoic porphyry-skarn Cu–Au–Mo–Fe deposits with reports of Pd, Pt, Se and Te enrichments (Gu and Chen, 1993; Wang et al., 2014; Xie et al., 2019a; Han et al., 2019). The Tongshankou deposit, as a representative porphyry-skarn Cu-Mo system in the region, has been reported to contain the highest Pd + Pt concentration of 20.8 ppb based on bulk ore assay results of 12 samples (Wang et al., 2020). Previous studies have suggested that the porphyry-skarn Cu-Mo (146–141 Ma) and Cu-Au (144–136 Ma) deposits in the Edong ore district are genetically related (Xie et al., 2011a b), yet the Pd, Pt, Se, and Te enrichment of Cu-Au deposits in the region have not been systematically studied. Preliminary prospecting of the Jiguanzui-Taohuazui deposit shows Se and Te enrichment, and estimated resources of 250 t Se and 122 t Te have been reported (Geological Team of Southeast Hubei Province, 1988). Based on these understandings, in this study we conducted bulk ore (and ore concentrate) analyses for base metal elements and PGE, in-situ electron probe microanalysis (EPMA) of Te- and Bi-bearing minerals, and laser ablation-inductively coupled plasma-mass spectrometry (LA-ICP-MS) of major sulfide minerals from the Jiguanzui-Taohuazui Cu-Au deposit in this region: (1) to investigate the distribution of Pd, Pt, Se and Te (2) to discuss the controlling factors on Pd, Pt, Se and Te mineralization, and (3) to compare the potential enrichment of Pd, Pt, Se and Te between porphyry-skarn Cu-Au and Cu-Mo deposits in the Edong ore district and elsewhere.

2. Regional geological setting

The Middle–Lower Yangtze River metallogenic belt is one of the most important igneous rock-related Cu-Fe-Au-Mo provinces in China, and is located along the northern margin of the Yangtze Craton and in the southeast of the North China Craton and Dabie orogenic belt (Mao et al., 2006, 2011; Xie et al., 2019b; Pan and Dong, 1999). To the northwest, the belt is bounded by the Xiangfan–Guangji fault (XGF), to the northeast by the Tangcheng–Lijiang regional strike–slip fault (TLF), and to the south by the Yangxin–Changzhou fault (YCF) (Fig. 1a). The belt comprises seven ore districts, including (from west to east) Edong, Jiurui, Anqing-guichi, Luzong, Tongling, Ningwu and Ningzhen, comprising over 200 polymetallic deposits. Three types of mineral deposits and associated magmatism have been recognized in the belt (Mao et al., 2011): (1) 148–135 Ma Cu polymetallic porphyry–skarn–stratabound deposits associated with high–K calc–alkaline granitoids intruded between 156 and 137 Ma; (2) 135–123 Ma magnetite–apatite deposits, associated with similarly aged gabbro, diorite, quartz diorite, quartz monzonite, granite, diorite porphyry intrusives, and their corresponding extrusive equivalents; and (3) a small number of uneconomic Cu-Au hydrothermal veins, associated with 127–123 Ma A–type granitoids and alkaline volcanic rocks. There are three major periods of tectonism in the Middle–Lower Yangtze River metallogenic belt: the formation of Precambrian metamorphic basement rocks; the formation of Cambrian-early Triassic submarine sedimentary rocks; and post-middle Triassic collisional orogenic and intercontinental deformation accompanied by volcaniclastic rocks (Zhai et al., 1992; Mao et al., 2011). The Permian and Triassic submarine sedimentary rocks are the host rocks for most of the porphyry-skarn deposits (Chang et al., 1991).

The Edong ore district is situated in the westernmost part of the Middle–Lower Yangtze River metallogenic belt. The intrusive rocks of the ore district are dominated by six batholiths (from north to south): Echeng, Tieshan, Jinshandian, Lingxiang, Yangxin and Yinzu (Fig. 1b). These consist of diorite, granodiorite, quartz diorite, monzonitic granite, and granite, and are surrounded or intruded by plenty of granite–-granodiorite porphyry stocks and mafic to intermediate dikes. Geochronological evidence suggests that these batholiths and stocks formed between the Late Jurassic and Early Cretaceous (Li et al., 2009, 2014; Xie et al., 2008, 2011b; Xie et al., 2012; Zhu et al., 2017; Li et al., 2019). Two episodes of magmatism and mineralization events were recognized by Xie et al. (2013), namely: (1) the formation of granodiorite, granite porphyry stocks, and diorite (147–136 Ma), and associated porphyry-skarn Cu-Mo deposits, Cu-Fe and Cu-Au skarn deposits (144–143 Ma); and (2) the formation of diorite, monzonitic granite, and granite (133–127 Ma), and related skarn Fe deposits (133–130 Ma). The main units exposed in the area include carbonates of the Triassic Daye Formation, sandy–shales of the Puqi Formation, coal–bearing sandy–-shales of the Jurassic Wuchang Formation, and volcanic–pyroclastic rocks of the Cretaceous Lingxiang and Dasi Formation (Xie et al., 2016; Duan and Jiang, 2018). Post-mineralization volcanic rocks are mainly preserved in the Jinniu basin, and comprise (from bottom to top) the Majiashan, Lingxiang and Dasi Formation (Xie et al., 2011b). Xie et al. (2008) established a metallogenic model of intra–continental porphyry–skarn Cu polymetallic deposits involving the formation of mineralizing intrusions from mixtures of an enriched mantle-derived mafic magma and a lower crust-derived felsic magma.

3. Deposit geology

The Jiguanzui-Taohuazui Cu-Au deposit sits on the northwest margin of the Yangxin batholith in the central Edong ore district, next to the large Tonglushan Cu-Au-Fe deposit (Fig. 1b). Sedimentary-volcanic strata exposed within the deposit comprise the dolomitic marble of Lower-Middle Triassic Jialingjiang Formation, Middle Triassic clastic rocks of the Puqi Formation, Early Cretaceous volcanic breccias of the Majiashan Formation, and volcanic rocks of the Cretaceous Lingxiang Formation. The mineralization is hosted by the Jialingjiang Formation marbles and the intrusion. The sedimentary host rocks were intruded by diorite and quartz diorite in the Jiguanzui-Taohuazui deposit along the major NE-trending Jiguanshan thrust faults (Fig. 2). Zircon U-Pb dating, molybdenite Re-Os dating and phlogopite Ar-Ar dating suggest the magmatic intrusion and hydrothermal mineralization at Tonglushan and Jiguanzui-Taohuazui are broadly coeval (140 to 137 Ma; Xie et al., 2011a). Furthermore, isotopic studies of the Late Jurassic and Early Cretaceous ore-forming magmatic intrusions indicate a similar origin of hybridization of enriched mantle derived mafic magma and variable amounts of ancient lower-crustal components (Xie et al., 2011b). Due to the discovery history, different names are given to the Jiguanzui and Taohuazui mining areas. However, given the nature of the causative intrusion, timing of mineralization, and their spatial proximity (Fig. 2), the two mining areas are regarded one deposit in this study.

The Jiguanzui mining area has been divided into seven mineralization zones (designated from #I to #VII), in which #III and #VII are the two major mineralization zones, with the #III mineralization zone located at the –22 to −530 mine levels, and the #VII mineralization zone located at the 700–1300 mine levels (Fig. 3a). The orebodies can be hosted in skarn alteration zones, in marble, inside the intrusion and in pelitic hornfels. The major mineralization occurs in the contact zones of the quartz diorite stock and carbonate sedimentary rocks, with both *endo*-skarn and *exo*-skarn alteration. Some orebodies also stretch out of the skarn and are hosted in a "bleached", hydrothermally altered, marble. Porphyry-type mineralization developed inside the intrusion in

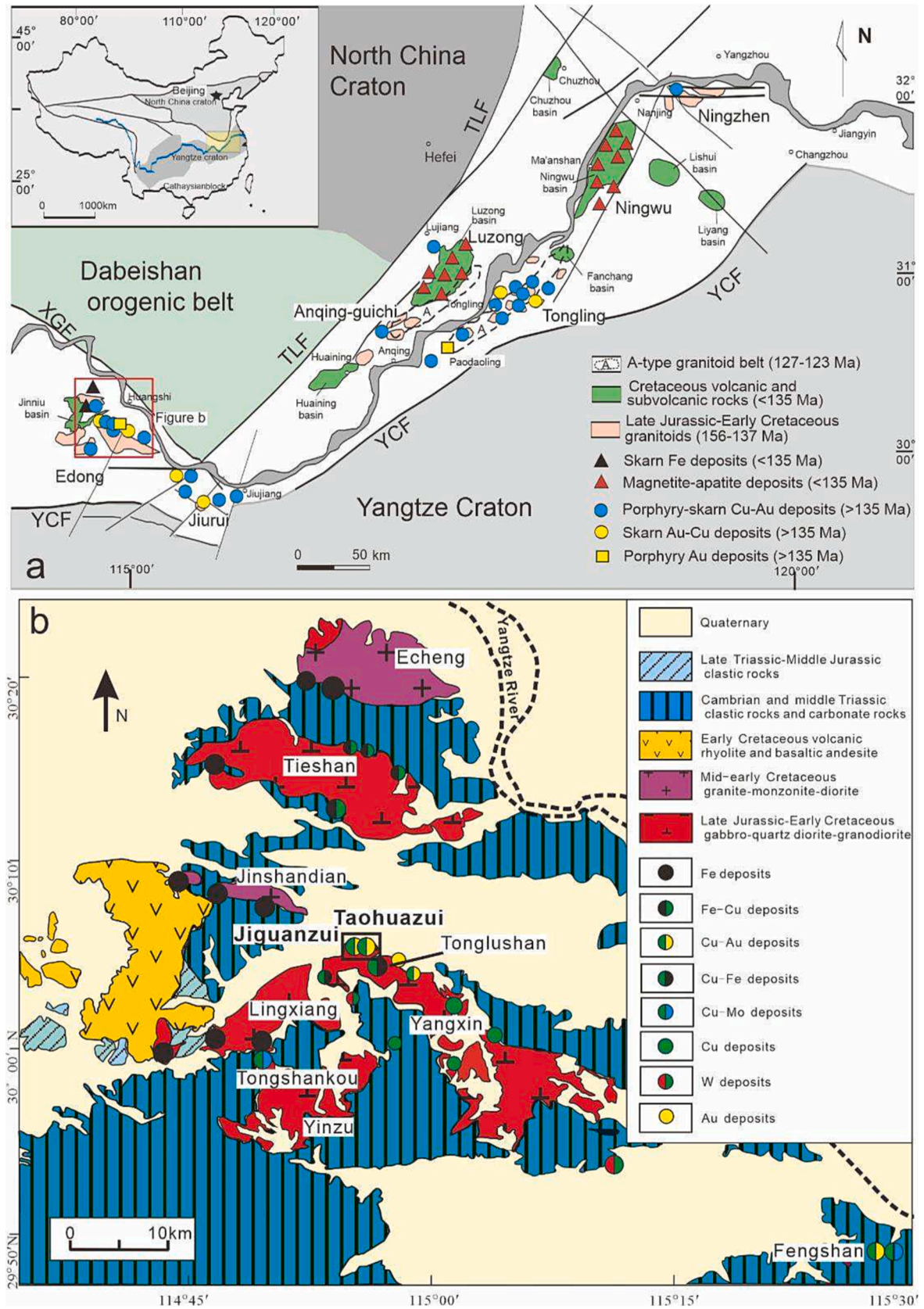

Fig. 1. (a) Location of the Edong ore district in the Middle–Lower Yangtze River metallogenic belt (MLYRB), Eastern China (modified after Mao et al., 2011); (b) Geologic map showing the major types of mineral deposits in Edong ore district (modified after Shu et al., 1992; Li et al., 2008; Xie et al., 2011a).

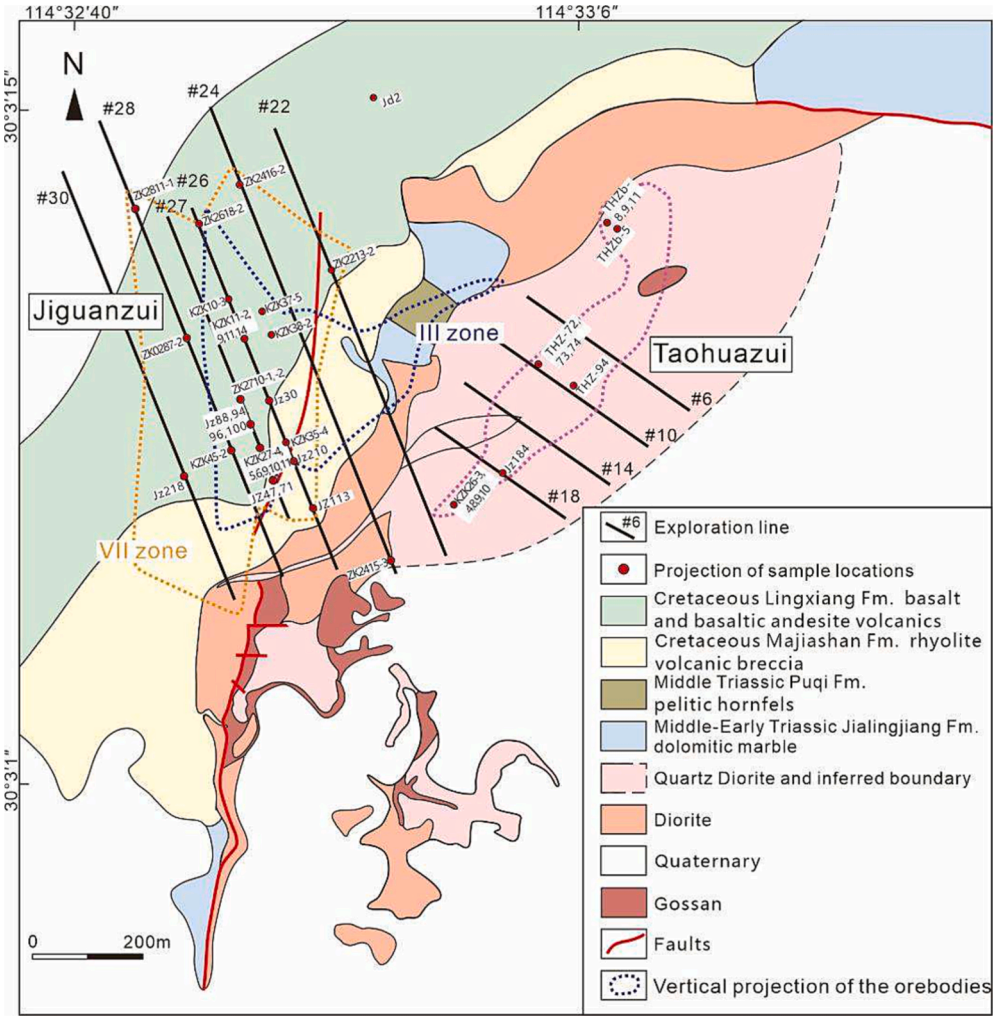

Fig. 2. Geologic map of the Jiguanzui-Taohuazui deposit with sampling locations in this study (modified from Geological Team of Southeast Hubei Province, 1988; Xie et al., 2011a). The #III and #VII mineralization zones of Jiguanzui are further shown in cross-sections in Fig. 3a.

places that do not have the skarn alteration assemblages and comprises quartz stockwork and calcite-quartz veins with pyrite and chalcopyrite associated with potassic alteration. These features generally have lower ore grades than the skarn mineralization and are volumetrically minor. Calcite and quartz veins with pyrite and chalcopyrite occur within the pelitic hornfels but are subeconomic. Metallic minerals in the Jiguanzui mining area include magnetite, pyrite, chalcopyrite, bornite, hematite, sphalerite and native gold (Fig. 4), and specific information of ore mineral assemblage classification through field and microscopic observation is displayed in section 5.1. Common alteration minerals include grandite garnet, pyroxene, epidote, K-feldspar, phlogopite, and chlorite in both the endo- and *exo*-skarn. The skarn-type mineralization/alteration at Jiguanzui has been divided into five stages by previous workers, namely: (1) prograde skarn, (2) retrograde, (3) iron oxide mineralization, (4) quartz - pyrite - chalcopyrite mineralization and (5) calcite - sulfide mineralization (Tian et al., 2019).

The mineralization in the Taohuazui mining area is similar to that of the nearby large Tonglushan deposit; the major orebodies are situated in relict marble units within the causative quartz diorite (Xie et al., 2011a; Fig. 3b). These marble xenoliths and orebodies are generally NE striking and NW trending, and they continue to depth; drill holes reveal that the host marble can still occur below −1200 levels (Fig. 2; Fig. 3b). The skarn, marble and the intrusion are the major host rocks for the mineralization in Taohuazui, whereas the pelitic hornfels are absent in this mining area. Compared to Jiguanzui, the Taohuazui mining area contains more magnetite ores, similar to the Tonglushan Cu-Au-Fe deposit (Xie et al., 2011a).

A previous microthermometric study at the Jiguanzui-Taohuazui deposit showed that the fluid inclusions in the skarn-hosted retrograde alteration minerals coexisting with the magnetite-sulfide assemblage consist predominately of brine inclusions that homogenize in the range of 530–380 °C (Zhang, 2015). Fluid inclusions associated with the major sulfide stage hosted by skarn and marble have ranges of 400–250 °C and 300–220 °C, respectively (Zhang, 2015).

4. Sampling and analytical methods

4.1. Sampling descriptions

Forty-eight ore samples from the Jiguanzui-Taohuazui deposit, including thirty-nine drill core samples and nine samples from adits were collected. Locations of the ore samples are listed in Appendix I. Four concentrate samples, including two iron concentrates and two copper–gold concentrates, were supplied by the flotation plant at Hubei Sanxin Gold & Copper Co., Ltd. The preliminary identification of the transparent and metallic minerals of the ore carried out during logging of the drill core and hand specimen description. Further studies petrographic studies using transmitted and reflected light microscopy were then completed.

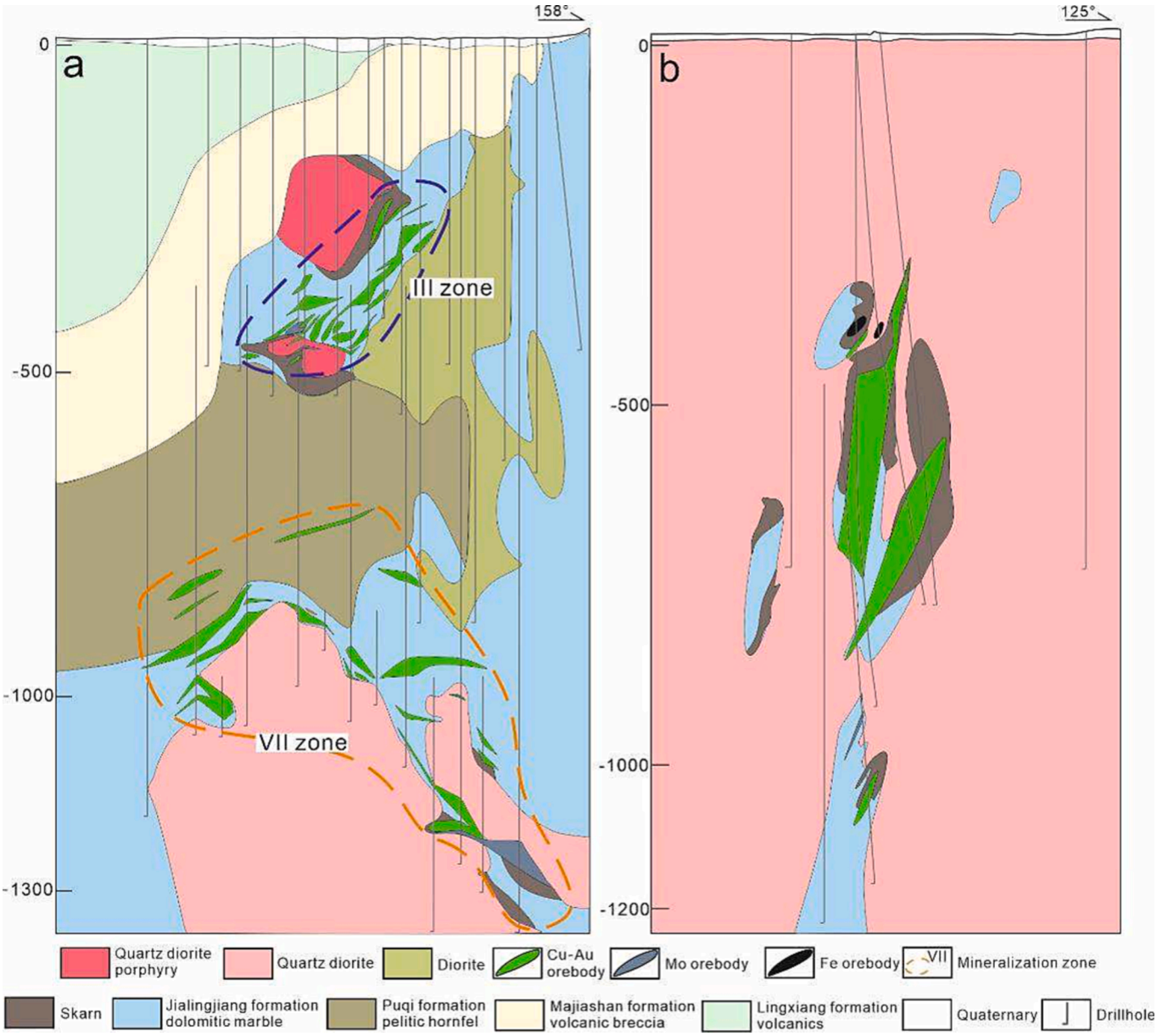

Fig. 3. Geological cross section of the Jiguanzui-Taohuazui Cu-Au deposit (modified after Ke et al., 2016). (a) the cross-section of #26 exploration line of the Jiguanzui mining area showing the main #III and #VII mineralization zones; (b) the cross-section of #10 exploration line of the Taohuazui mining area.

4.2. Bulk ore major and minor elements assay

Platinum, Pd, Au, Se and Te contents were determined at Australian Laboratory Services (ALS) CHEMX, Guangzhou, China. After pre-concentration by the Lead Fire Assay technique from 30 g ore concentrate samples or 60 g of ore samples, Pd, Pt and Au were determined using an ICP–MS method (ALS CHEMX code: PGM–MS23L with relative difference (RD) calculated from the analysis of external standards calculated from duplicate analyses < 10 % and relative error (RE) < 6 %). The detection limits were 0.1 ppb for Pt, 0.2 ppb for Pd and 1 ppb for Au. Selenium and Te concentrations were determined using a combination of ICP–MS and ICP–OES methods (ALS CHEMX code: ME–MS61; RD < 10 %, RE < 10 %) with detection limits of 1 ppm for selenium and 0.05 ppm for tellurium. Low selenium content samples were digested first by HNO_3 and then HCl, then determined by ICP–MS method (ALS CHEMX code: SE–MS46; RD < 15 %, RE < 10 %) with detection limits of 0.05 ppm.

Base metal and other trace elements were determined by ICP–MS at the Australian Laboratory Services (ALS) CHEMX, Guangzhou, China (ALS CHEMX code: ME–ICP61a; RD < 7.07 %, RE < 7.07 %). Detection limits are 20 ppm for Bi, 10 ppm for Cu and 0.05 wt% for S. For samples with Cu contents above 10 wt%, ALS CHEMX code Cu–VOL61 (RD $<$ 3.54 %, RE < 2.5 %) and S–IR08 (RD < 5 %, RE < 3.54 %) are employed to determine Cu and S contents, with detection limits of 0.01 wt% for both elements.

4.3. In-situ major and trace element analysis

The compositions of accessory Bi-,Te- and Se- bearing minerals were determined using a JOEL JXA–8230 electron microprobe at the Key Laboratory of Metallogeny and Mineral Assessment, Institute of Mineral Resources, Chinese Academy of Geological Sciences (CAGS), Beijing. The operating conditions are: accelerating voltage of 20 kV, beam current of 20nA, and beam diameter of 1 μm. The counting time was 10 s on the peak, and 5 s each on left–hand and right–hand background position for each element. The detection limits were 492 ppm for Au, 220 ppm for

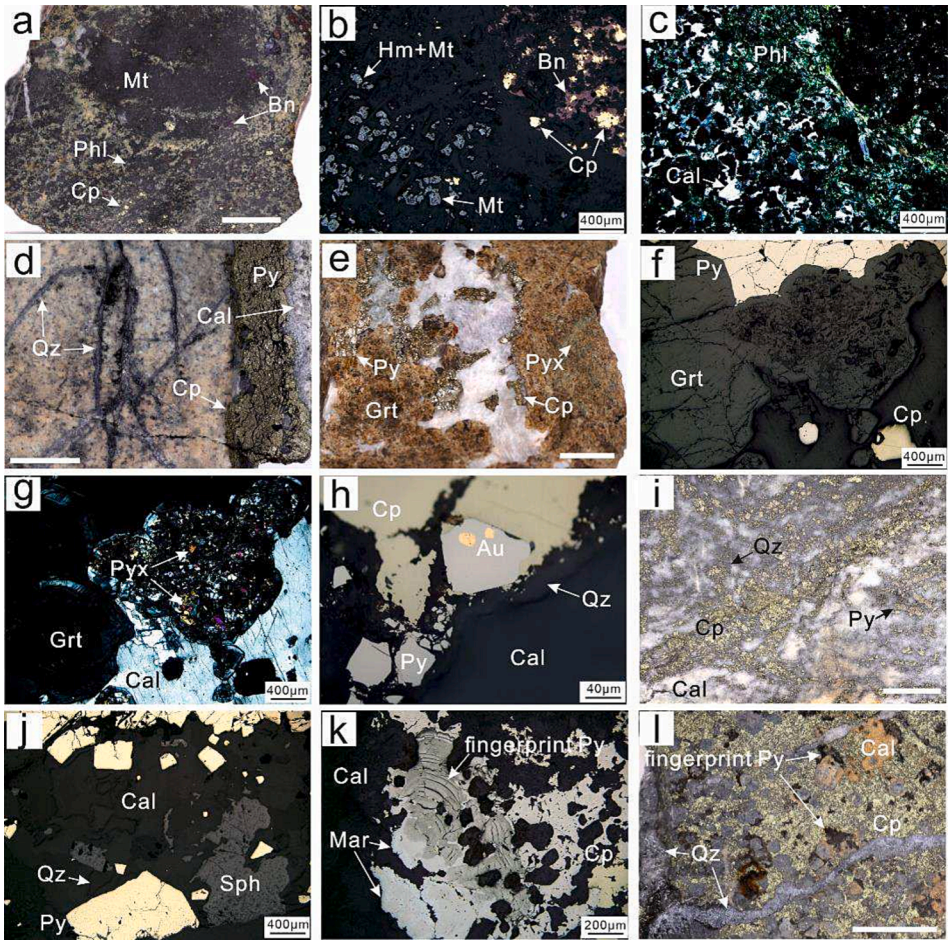

Fig. 4. Photographs and photomicrographs of major ore mineral assemblages in Jiguanzui-Taohuazui. White scale bars are 1 cm unless indicated otherwise. a: Mt-Bn-Cp-Hm assemblage coexisting with retrograde phlogopite from the *endo*-skarn alteration zone; b, c: photomicrograph of Mt-Bn-Cp-Hm assemblage with coexisting phlogopite; d: porphyry type ore of Cp-Py assemblage; e: Cp-Py assemblage from the *exo*-skarn alteration zone; f, g: photomicrograph of Cp-Py assemblage in *exo*-skarn; h: inclusions of native gold in Cp-Py assemblage from *exo*-skarn; i: Py-Cp-Sph assemblage in marble; j: photomicrograph of Py-Cp-Sph assemblage in marble; k: photomicrograph of fingerprint textured pyrite in Py-Cp-Sph assemblage in marble; l: dark-coloured "fingerprint" textured pyrite in marble in hand specimen. Abbreviations: Au-native gold; Bn-bornite; Cal-calcite; Cp-chalcopyrite; Ep-epidote; Grt-garnet; Hm-hematite; Mar-marcasite; Mt-magnetite; Phl-phlogopite; Py-pyrite; Pyx-pyroxene; Qz-quartz; Sph-sphalerite.

Ag, 286 ppm for Bi, 364 ppm for Te, and 178 ppm for Se. Natural and synthetic mineral standards of chalcopyrite, pyrite, sphalerite, galena, CoNiAs, SnO2, MnTi, and native Ag, Sb, Au, Se, Te, and Cd were used for calibration, and ZAF corrections were made with proprietary JEOL software.

LA-ICP-MS was conducted on pyrite, bornite, and chalcopyrite to determine the concentration of PGE, and on pyrite, bornite, chalcopyrite, and sphalerite to determine major and trace elements present in those sulfides at the State Key Laboratory of Ore Deposit Geochemistry, IGCAS, using an Agilent 7700 × quadrupole ICP-MS coupled to an ASI RESOLution-LR-S155 laser microprobe equipped with a Coherent Compex-Pro 193 nm ArF excimer laser. A laser beam of 26 μm was used with a pulse rate of 5 Hz and a fluence of 2.7 J/cm^2 for PGE analyses, and a fluence of 3 J/cm^2 for major and trace elements analyses. Ablation was performed in a He atmosphere flowing at 0.35 L/min. The ablated aerosol was mixed with Ar (1.05 L/min) for PGE analyses and with Ar (900 ml/min) for major and trace element analyses as a transport gas. The following isotopes measured were:^{34}S, ^{55}Mn, ^{57}Fe, ^{59}Co, ^{60}Ni, ^{65}Cu, ^{66}Zn, ^{75}As, ^{77}Se, ^{93}Nb, ^{99}Ru, ^{103}Rh, ^{106}Pd, ^{109}Ag, ^{111}Cd, ^{118}Sn, ^{121}Sb, ^{125}Te, ^{185}Re, ^{189}Os, ^{193}Ir, ^{195}Pt, ^{197}Au, ^{206}Pb, ^{209}Bi. At mean time, ^{87}Sr, ^{90}Zr, ^{92}Zr, ^{181}Ta were monitored to handle the potential interferences for PGE analyses. Total acquisition time for each analysis was 90 s, comprising 30 s of gas background and 60 s of ablation signal. Signal quantification was carried following the standard methods (Longerich et al., 1996; Kosler, 2001). For PGE analyses, Po724-T (Sylvester et al., 2005), NiS_3 (Gilbert et al., 2013) and STDGL2b2 (Danyushevsky et al., 2011) reference materials were used for calibration. Oxidation yield ThO/Th < 0.1 was an important tuning parameter. And to confirm the contribution of oxygen, ^{29}Si and ^{45}Sc in quartz (in-house standard) were analyzed three times per hour during the whole test work. The interferences could be ^{61}Ni^{40}Ar interferences on ^{101}Ru, ^{59}Co^{40}Ar on ^{99}Ru, ^{63}Cu^{40}Ar on ^{103}Rh, ^{65}Cu^{40}Ar on ^{105}Pd, and ^{66}Zn^{40}Ar on ^{106}Pd. The production of extent of base metal-argide were determined by ablating pure Co, Ni, Cu and Zn, and a correction factor was applied to the results to quantification the Ru, Rh and Pd. By recording the signal of ^{111}Cd, the isobaric interference of ^{106}Cd on ^{106}Pd were corrected. For major and trace element analyses, STDGL3 was used to determine concentrations of chalcophile and siderophile elements (Danyushevsky et al., 2011), and the in-house standard pure pyrite Py was used for calibration the concentrations of S. The integrated count data to concentrations for lithophile elements were calibrated and converted by GSD-1G. Sulfide reference material MASS-1 was analyzed as an unknown sample to check the analytical accuracy.

5. Results

5.1. Mineral assemblages

Using petrography, three groups of ore mineral and alteration assemblages were classified on the basis of their sulfide and oxide mineralogy. (1) A magnetite-bornite-chalcopyrite-(hematite) (Mt-Bn-Cp-Hm) assemblage intimately coexisting with retrograde minerals, especially phlogopite (Fig. 4a-c) although hematite also occurs in some samples of this assemblage. This assemblage occurs along the contact zones between the intrusion and the country rock, and can be hosted in both *endo*-skarn and *exo*-skarn. (2) A chalcopyrite-pyrite (Cp-Py) assemblage hosted in the intrusion (porphyry-type mineralization) and the exoskarn (Fig. 4d-h). This assemblage typically coexists with epidote, chlorite, quartz, and calcite. (3) A pyrite-chalcopyrite-(sphalerite) (Py-Cp-Sph) assemblage hosted by marble with elevated

marcasite contents in the northern part of #24, #26 and #28 exploration lines (Figs. 2 and 4i j). This mineral assemblage usually coexists with calcite and quartz. Pyrite with unusual "fingerprint" textures was also identified by optical microscopy in the Py-Cp-Sph and Cp-Py assemblages (Fig. 4k); these pyrites are usually dark-coloured in hand specimen (Fig. 4l).

5.2. Bulk ore Pd, Pt, Se and Te abundance

Bulk ore base metal elements and PGE contents are listed in Table 1. The average Pd, Pt, Se, Te and Au concentrations were determined for the three different types of ore assemblages, with 22.89 ppb, 1.77 ppb, 19.1 ppm, 2.69 ppm and 3.19 ppm, respectively in the Mt-Bn-Cp-Hm assemblage; 1.95 ppb, 0.35 ppb, 6.52 ppm, 14.75 ppm, and 2.03 ppm, respectively in the Cp-Py assemblage and 2.38 ppb, 1.02 ppb, 35.64 ppm 22.6 ppm and 5.26 ppm, respectively in the Py-Cp-Sph assemblage. The

Table 1
Chemical analyses of major (Cu, S; wt. %) and trace (ppm) element contents of samples from the Jiguanzui-Taohuazui deposit. Elements with * are in ppb.

Types of samples	Sample numbers	Bi	Cu	S	Au*	Pd*	Pt*	Te	Se	Te/S	Se/S	Pd + Pt	R_{Pd-Cu}
Mt-Bn-Cp-Hm assemblage	THZ74	30	13.54	18.45	14,900	53.2	1.3	6.8	50	0.37	2.71	54.5	0.68
	JZ100	20	3.27	5.6	3420	18.3	3.4	1.3	20	0.23	3.57	21.7	
	JZ71	<20	0.39	0.63	194	5.3	1.1	0.24	2	0.38	3.17	6.4	
	TKZK26-10	30	5.14	9	2580	66.9	1.5	2.6	10	0.29	1.11	68.4	
	KZK27-4	20	0.09	7.48	107	23.6	3.9	0.8	18	0.11	2.41	27.5	
	JZ96	<20	3.62	5.59	n.a.	5.9	1.3	1.7	30	0.30	5.37	7.2	
	TKZK26-4	20	8.42	8.5	n.a.	n.a.	n.a.	2.7	30	0.32	3.53	–	
	KZK27-5	<20	0.10	1.98	290	3.6	0.4	1.82	3	0.92	1.52	4	
	KZK27-10	20	1.22	7.06	n.a.	5.2	0.3	8.45	22	1.20	3.12	5.5	
	kzk45-2	<20	0.79	1.44	823	24	2.7	0.45	6	0.31	4.17	26.7	
	avg	14.00	3.66	6.57	3187.71	22.89	1.77	2.69	19.10	0.44	3.07	24.66	
	max	30	13.54	18.45	14,900	66.9	3.9	8.45	50	1.20	5.37	68.4	
	min	–	0.09	0.63	107	3.6	0.3	0.24	2	0.11	1.11	4	
Cp-Py assemblage	TKZK26-3	<20	1.18	1.48	946	13.4	1.8	0.48	4.7	0.32	3.18	15.2	0.00
	TKZK26-8	<20	0.26	1.37	132	<0.2	0.1	0.81	1.695	0.59	1.24	0.1	
	JZ88	460	0.31	2.03	n.a.	0.6	0.3	147.5	7	72.66	3.45	0.9	
	KZK11-9	<20	0.17	1.77	172	2.4	0.2	7.35	2.67	4.15	1.51	2.6	
	KZK11-11	30	0.01	2.01	16	<0.2	0.1	11.35	3.99	5.65	1.99	0.1	
	JZ184	<20	0.01	0.11	7	<0.2	0.1	<0.05	0.176	–	1.60	0.1	
	KZK27-9	20	0.18	0.31	297	1.2	0.1	0.96	2	3.10	6.45	1.3	
	KZK27-6	<20	0.51	1.82	n.a.	2.3	0.4	1.32	5	0.73	2.75	2.7	
	JZ113	20	0.03	2.71	n.a.	n.a.	n.a.	0.7	10	0.26	3.69	–	
	ZK2710-1	20	0.05	0.15	720	0.3	0.2	0.15	1	1.00	6.67	0.5	
	THZ73	<20	0.04	0.06	6	<0.2	0.1	<0.05	0.053	0.00	0.88	0.1	
	THZ94	30	15.70	16.8	15,950	1.2	0.4	6.4	40	0.38	2.38	1.6	
	avg	48.33	1.54	2.55	2027.33	1.95	0.35	14.75	6.52	7.40	2.98	2.29	
	max	460	15.70	16.8	15,950	13.4	1.8	147.5	40	72.66	6.67	15.2	
	min	–	0.01	0.06	6.00	–	0.10	–	0.053	–	0.88	0.10	
Py-Cp-Sph assemblage	ZK2811-1	20	0.01	6.1	11	0.6	0.4	0.18	1	0.03	0.16	1	0.35
	ZK2710-2	15,400	3.03	39	n.a.	n.a.	n.a.	27.4	50	0.70	1.28	–	
	ZK2618-2	80	0.03	28.4	n.a.	0.7	0.7	16.05	19	0.57	0.67	1.4	
	ZK2416-2	40	0.01	35.5	n.a.	0.5	0.7	22.8	14	0.64	0.39	1.2	
	ZK2415-3	70	11.94	13.2	16,350	23.4	2	10.8	80	0.82	6.06	25.4	
	ZK2213-2	60	0.02	11.75	n.a.	1.4	0.6	29.6	48	2.52	4.09	2	
	ZK0287-2	400	0.34	22.6	n.a.	1.1	0.9	54.2	50	2.40	2.21	2	
	kzk38-2	20	0.55	12.2	162	1.1	0.7	0.47	13	0.04	1.07	1.8	
	kzk37-5	20	14.70	18.95	n.a.	0.7	0.6	3.3	70	0.17	3.69	1.3	
	KZK35-4	20	4.78	27.6	n.a.	1.1	0.8	3	50	0.11	1.81	1.9	
	KZK27-11	30	3.98	12.7	7920	3.8	1	11.7	40	0.92	3.15	4.8	
	KZK10-3	120	0.10	45.4	186	0.5	1.2	29.8	126	0.66	2.78	1.7	
	JZ94	20	0.17	41.4	n.a.	n.a.	n.a.	2.8	10	0.07	0.24	–	
	JZ47	160	21.01	29.5	28,300	1.5	1	72.9	90	2.47	3.05	2.5	
	JZ30	40	0.01	17.05	145	0.3	0.3	9.12	7	0.53	0.41	0.6	
	JZ218	350	0.01	47.3	6910	1.2	0.9	249	92	5.26	1.95	2.1	
	JZ210	20	1.05	43.2	n.a.	n.a.	n.a.	0.34	50	0.01	1.16	–	
	KZK11-2	30	6.57	13.45	8230	0.9	0.7	4.1	30	0.30	2.23	1.6	
	KZK11-14	30	0.03	4.69	66	0.5	0.7	14.45	4.56	3.08	0.97	1.2	
	JD2	20	0.01	5.82	81	<0.2	0.2	0.43	1	0.07	0.17	0.2	
	THZb5	<20	0.06	0.4	108	2.5	1.7	0.05	0.172	0.13	0.43	4.2	
	THZb8	20	5.44	21.8	7350	5.2	1.6	4.7	30	0.22	1.38	6.8	
	THZb9	<20	0.65	1.55	559	1.8	0.2	0.28	2.27	0.18	1.46	2	
	THZb11	20	9.94	8.46	9740	2.5	5.9	5.1	40	0.60	4.73	8.4	
	THZ72	20	1.55	n.a.	2340	1.9	0.5	10.75	0.026	–	–	2.4	
	TKZK26-9	50	1.99	3.15	1025	1.6	0.2	4.22	8.74	1.34	2.77	1.8	
	avg	656.15	3.38	20.45	5263.71	2.38	1.02	22.60	35.64	0.95	1.93	3.40	
	max	15,400	21.01	47.3	28,300	23.4	5.9	249	126	5.26	6.06	25.4	
	min	–	0.01	0.4	11	–	0.2	0.05	0.026	0.01	0.16	0.2	
Flotation concentrates	Cu-Au 1	60	18.46	35.4	20,300	34.6	3.5	18.5	70	–	–	38.10	–
	Cu-Au 2	70	19.01	36.4	22,600	36.1	3.5	18.8	70			39.60	
	avg	65	18.74	35.9	21,450	35.35	3.5	18.65	70			–	
	Fe 1	<20	0.06	0.23	119	2.1	0.9	0.24	0.30			3.00	
	Fe 2	<20	0.03	0.16	64	1.5	0.8	0.18	0.21			2.30	
	avg	–	0.05	0.20	91.5	1.8	0.85	0.21	0.25			–	

range and median concentration of the three types of ore and variations of Pd, Pt, Se and Te contents of different mineral assemblages are shown in Fig. 5a-d. The highest concentration of Pd + Pt occurs in the Mt-Bn-Cp-Hm assemblage (68.4 ppb), which has moderate Au concentrations (averaging 3.19 ppm), and the highest contents of Se and Te come from the Py-Cp-Sph assemblage (126 ppm and 249 ppm, respectively), which is Au rich (averaging 5.26 ppm) (Table 1). Elevated Se and Te values were often identified in samples with high S concentrations, especially in massive sulfide ore, therefore, the Se/S and Te/S values were calculated to normalize the effect of high sulfide concentrations on Se and Te contents. Selenium/S values show declining trends in the order of the Mt-Bn-Cp-Hm, Cp-Py, and Py-Cp-Sph assemblages, whereas no significant variations of Te/S ratios among the three assemblages are shown in the figure (Fig. 5e-f). For the four concentrate samples analyzed, the Cu-Au sulfide concentrates contain average contents of 35.4 ppb Pd, 3.5 ppb Pt, 70 ppm Se and 18.7 ppm Te, and the Fe concentrates contain average contents of 1.8 ppb Pd, 0.9 ppb Pt, 0.3 ppm Se and 0.2 ppm Te (Table 1; Fig. 7).

5.3. Correlation between critical metals and associated elements

A correlation (r value) matrix was calculated for selected elements (Cu, S, Au, Pd, Pt, Te, Se) and indicates moderate Pd-Cu, Pd-Pt, Se-Te, Te-S and Te-Au associations and positive correlations between Au-Cu, Se-S, and Se-Au (Table 2). Mathematical calculation and covariant diagrams for Cu, S, Au and critical metals (Pd, Pt, Se, Te) from the three assemblages from Jiguanzui-Taohuazui (Fig. 6) show that (1) excluding the separate six "high Cu low Pd samples", Pd and Cu are positively correlated (r = 0.68) (Fig. 6a); (2) both Se and Te concentrations are broadly correlated with S contents (Fig. 6h, i).

Table 2
Correlation matrix of r values for associated elements from the Jiguanzui-Taohuazui deposit.

	Cu	S	Au	Pd	Pt	Te	Se
Cu	1						
S	0.18	1					
Au	0.96	0.48	1				
Pd	0.26	−0.05	0.18	1			
Pt	0.23	0.03	0.20	0.36	1		
Te	−0.01	0.40	0.28	−0.13	−0.07	1	
Se	0.53	0.71	0.64	0.04	0.20	0.42	1

5.4. The occurrence of telluride and sulfosalt minerals

Abundant Bi-Te-Se minerals have been observed in some of the Te-rich Py-Cp-Sph assemblage samples. Unnamed Bi-Te-Se minerals alone, or together, with wittichenite (Cu_3BiS_3) occur along the cracks of pyrite crystals in these samples (Fig. 8). Minor cervelleite (Ag_4TeS) have been observed in the Mt-Bn-Cp-Hm assemblage, and it intimately co-exists with bornite (Fig. 8). EPMA results of these minerals are listed in Table 3.

5.5. In-situ LA-ICP-MS analyses of sulfide minerals

The PGE concentrations of twelve sulfide mineral samples from the PGE-rich Mt-Bn-Cp-Hm assemblage are listed in Table 4. Relatively high Pd contents were identified in pyrite (up to 0.48 ppm), with four of the

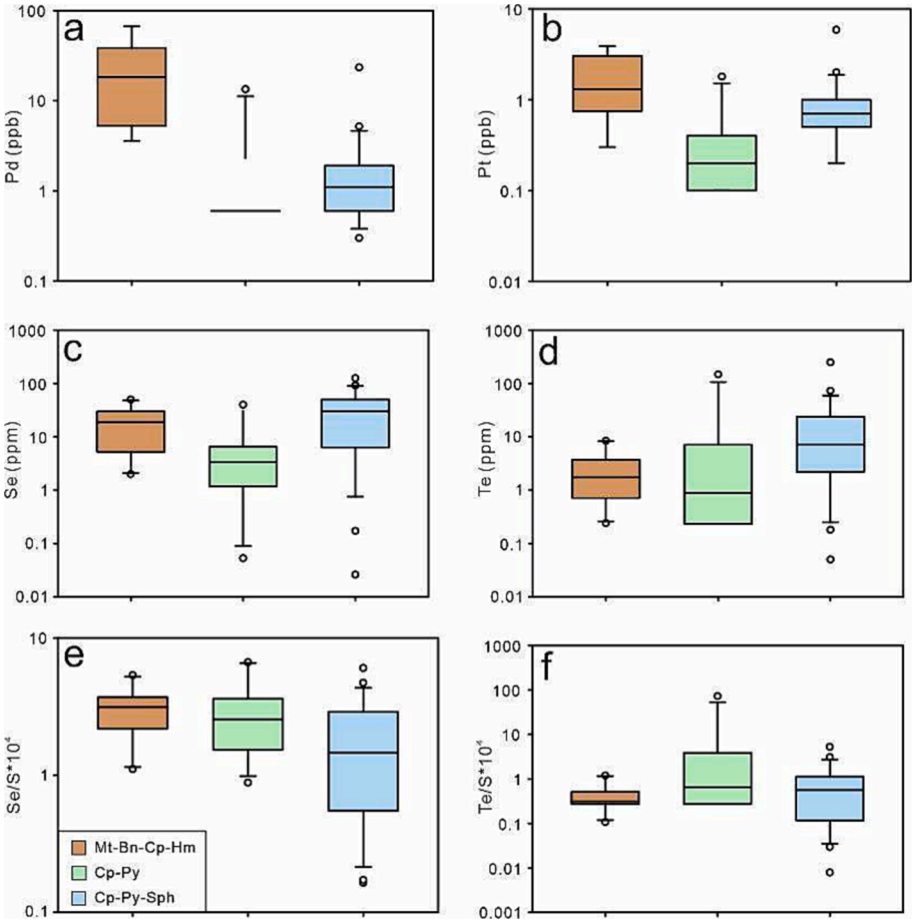

Fig. 5. Box diagram of Pd, Pt, Se and Te concentrations for the three major types of ore from Jiguanzui-Taohuazui. To normalize the effect of high sulfide contents on Se and Te contents, ranges of Se/S and Te/S values are shown in (e) and (f).

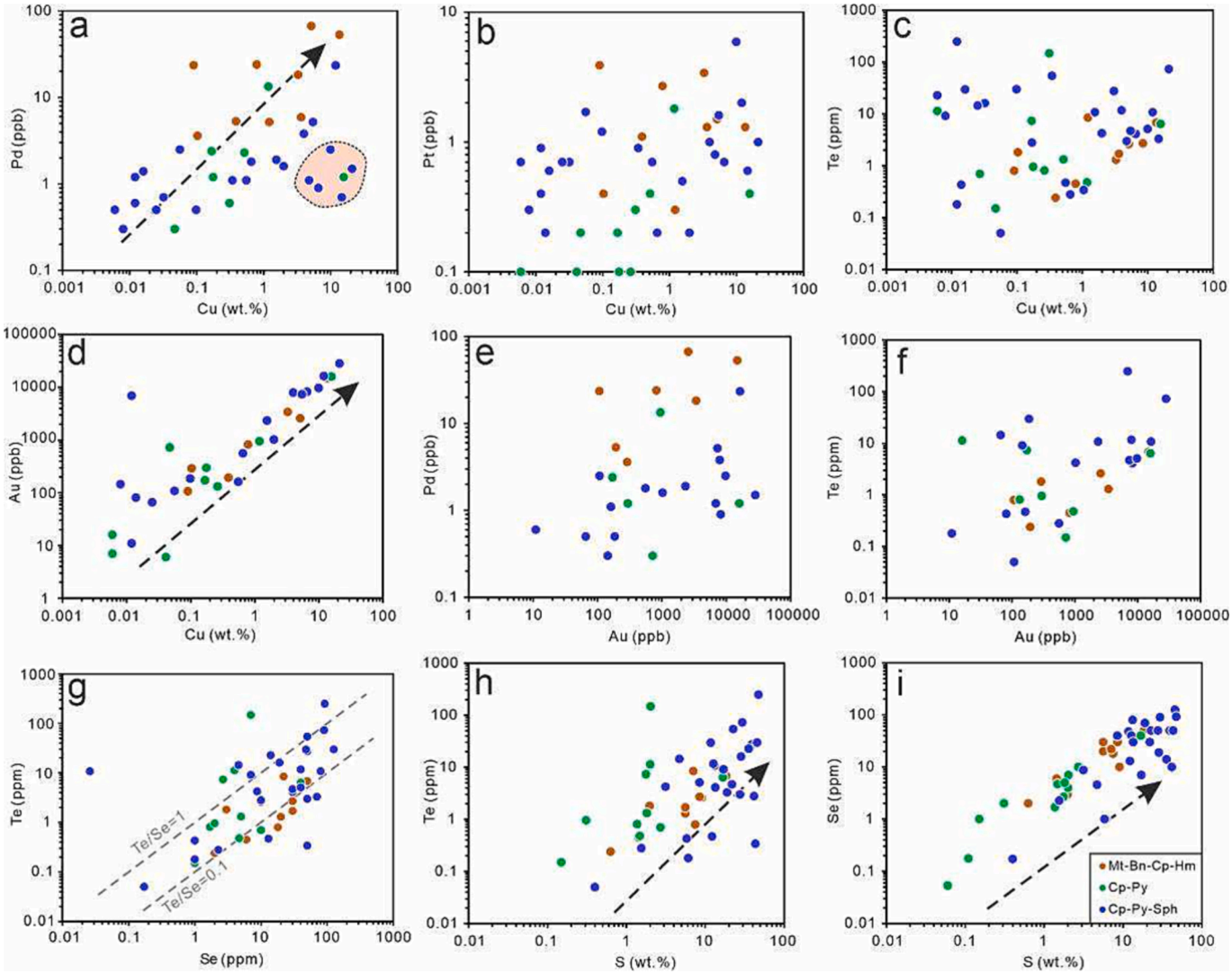

Fig. 6. Covariant diagrams of Cu, Au, S with Pd, Pt, Se and Te of the three ore mineral assemblages from the Jiguanzui-Taohuazui deposit. (a-d) Cu vs Pd (a), Pt (b), Te (c) and Au (d); (e-f) Au vs Pd (e) and Te (f); (g) Se vs Te showing Te/Se ratios; (h-i) S vs Te (h) and Se (i). The coloured field in (a) is the "high Cu low Pd" group in which the "fingerprint" textured pyrites develop.

five analyses results above the detection limits, whereas the Pd contents of bornite and chalcopyrite are below, or near, the detection limits (Table 4). Platinum is mainly hosted in pyrite, with a maximum value of 0.15 ppm. The Cu sulfides, namely chalcopyrite and bornite, return Pt contents below the detection limits.

Twenty-six trace element results of sulfide minerals from the three assemblages are listed in Table 5, and the Se and Te contents of the sulfides are shown in Fig. 9. Generally, sulfides from the Mt-Bn-Cp-Hm and the Py-Cp assemblages return higher Se contents (34 ~ 130 ppm), whereas sulfides from the Py-Cp-Sph assemblage typically return low Se contents (0.9 ~ 39 ppm). Tellurium contents are low in all sulfide minerals (below detection limit to 2.89 ppm) except for the three results of pyrite from the sample with abundant Bi-Te-Se minerals from the Py-Cp-Sph assemblage (averaging 105.5 ppm, Table 5; Fig. 9).

6. Discussion

6.1. Distribution and hydrothermal transport of Pd and Pt

Analytical results of bulk ore samples from the Jiguanzui-Taohuazui deposit show the highest Pd + Pt contents in the Mt-Bn-Cp-Hm assemblage (averaging 22.2 ppb with maximum of 68.4 ppb) from the skarn zones. No PGE bearing minerals have been identified in this study by optical or EPMA imaging using backscattered electrons. A previous study on the Kalmakyr porphyry Cu deposit in Uzbekistan suggested that Pd was dominantly hosted by Cu-bearing sulfides (Pašava et al., 2010). However, in this study the LA-ICP-MS data show that pyrite is the major host for both Pd and Pt (Table 4), and therefore, the dominance of Cu-bearing minerals in the Mt-Bn-Cp-Hm assemblage is not the reason for its elevated PGE contents. Given the measured fluctuations in Pd and Pt contents in pyrite, it is assumed that the PGE are present in nano-inclusions, however, further nano-scale studies are required to confirm this.

Microthermometric studies (Zhang, 2015) suggest that the retrograde alteration minerals coexisting with the Mt-Bn-Cp-Hm assemblage formed at high temperatures (530 ~ 380 °C) and high salinities. This stage is dominated by brine inclusions (40 ~ 65 wt% NaCl eqv.), and the salinities of the liquid-rich inclusions range from 15 ~ 25 wt% NaCl eqv. The Cp-Py assemblage (400 ~ 250 °C), widely associated with quartz and calcite, and the Py-Cp-Sph (300 ~ 220 °C) assemblage in marble formed at lower temperatures and salinities. This features more liquid rich inclusions, with salinities ranging from 40 ~ 54 wt% NaCl eqv. for the brine inclusions and 16 ~ 24 wt% NaCl eqv. for the liquid-rich inclusions in the Cp-Py assemblage, and absence of brine inclusions and

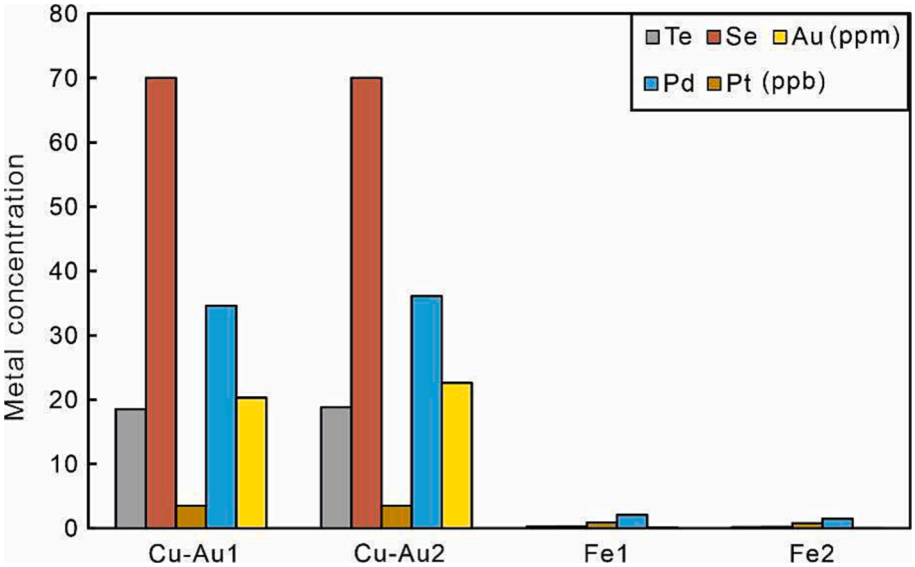

Fig. 7. Palladium, Pt, Se and Te concentrations of Cu-Au and Fe concentrates from the Jiguanzui-Taohuazui deposit. Cu-Au1and Cu-Au2 are copper gold sulfide concentrates; Fe1 and Fe2 are iron oxide concentrates.

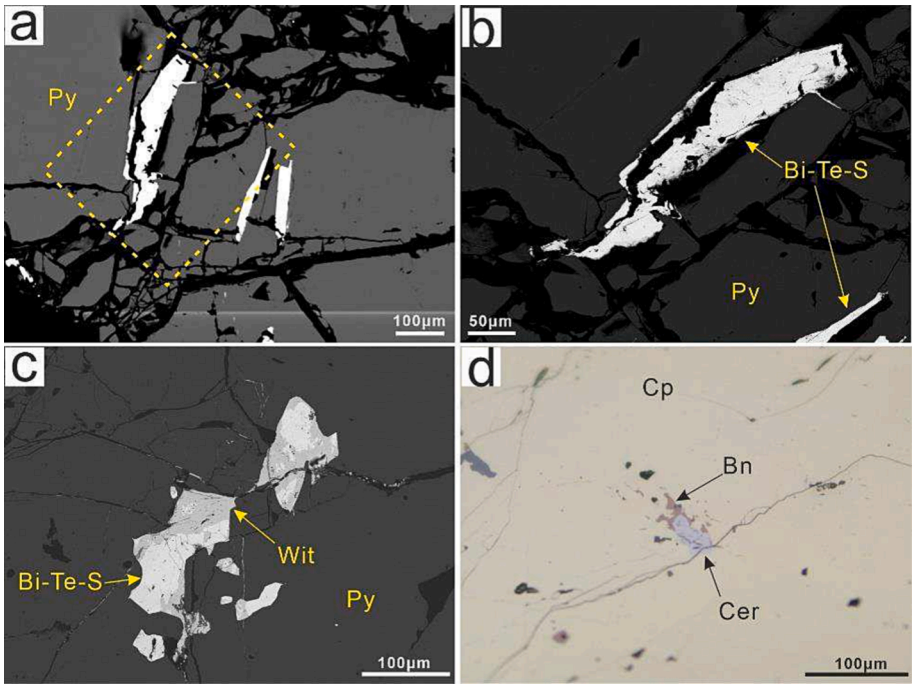

Fig. 8. Photomicrographs of Te-bearing minerals at Jiguanzui-Taohuazui deposit. a, b: unnamed Bi-Te-S minerals occur in the cracks of pyrite; c: unnamed Bi-Te-S minerals coexisting with wittichenite in the cracks of pyrite; d: cervelleite (Ag_4TeS) and bornite mineral inclusion in chalcopyrite. Bn-bornite; Cer-cervelleite; Cp-chalcopyrite; Py-pyrite; Wit- wittichenite.

Table 3
EPMA data of telluride and sulfosalt minerals from the Jiguanzui-Taohuazui deposit.

Spot	Mineral	Te	Bi	Cu	Ag	S	Se	Fe	Pb	Au	Zn	As	Total
JZ218-1	Bi-Te-S	43.73	48.59	0.06	0.07	4.78	0.67	1.12	b.d.	b.d.	0.05	b.d.	99.06
JZ218-2	Bi-Te-S	42.21	51.38	0.00	0.10	4.68	0.57	0.68	b.d.	b.d.	b.d.	b.d.	99.61
JZ218-3	wittichenite	0.00	38.12	37.60	0.30	19.66	0.05	2.54	b.d.	0.05	0.03	b.d.	98.35
JZ218-4	wittichenite	0.00	37.83	40.61	0.95	19.43	0.03	0.51	b.d.	0.05	b.d.	b.d.	99.42
THZ94-1	cervelleite	19.34	0.07	3.84	72.23	5.78	0.20	1.03	b.d.	b.d.	b.d.	b.d.	102.49
THZ94-2	cervelleite	19.02	0.00	3.52	69.92	5.68	0.28	1.20	b.d.	b.d.	0.01	b.d.	99.61

Table 4
PGE and Au contents of sulfide minerals from the Jiguanzui-Taohuazui deposit.

Analysis	Pd	Pt	Au	Mineral
JZ100-py-1	b.d.	0.15	b.d.	pyrite
JZ100-py-2	0.01	0.03	b.d.	pyrite
JZ100-py-3	0.43	b.d.	b.d.	pyrite
JZ100-py-4	0.06	0.11	0.02	pyrite
JZ100-py-5	0.48	b.d.	b.d.	pyrite
JZ100-bn-1	0.01	b.d.	b.d.	bornite
JZ100-bn-2	b.d.	b.d.	b.d.	bornite
JZ100-bn-3	0.04	b.d.	b.d.	bornite
JZ100-cp-1	b.d.	b.d.	0.04	chalcopyrite
JZ100-cp-2	0.07	b.d.	b.d.	chalcopyrite
JZ100-cp-3	0.01	b.d.	b.d.	chalcopyrite
JZ100-cp-4	b.d.	b.d.	0.01	chalcopyrite

19 ~ 23 wt% NaCl eqv. for liquid-rich inclusions in the Py-Cp-Sph assemblage. These two latter mineral assemblages generally have much lower Pd + Pt concentrations (averaging 2.3 ppb for Cp-Py and 3.4 ppb for Py-Cp-Sph, Table 1). Therefore, although the salinity of the fluid is likely an important factor for the transport and precipitation of PGE, the temperature may be the main control. Previous case studies on PGE-rich porphyry-skarn systems indicate that high PGE contents (up to ppm levels) are generally found in the magnetite-bearing assemblages of potassic alteration zones, proximal to centers of magmatic hydrothermal systems and which represent the early high temperature stages dominated by magmatic-hydrothermal fluids (Economou-Eliopoulos, 2005; John and Taylor, 2016). For example, PGE are strongly enriched in a magnetite-bearing bornite-chalcopyrite assemblage (averaging 40 ppb Pd and 16 ppb Pt) associated with potassic alteration in the Elatsite porphyry Cu deposit in Bulgaria, but a chalcopyrite-pyrite assemblage associated with sericitic alteration had much lower PGE concentrations (averaging 14 ppb Pd and 3.6 ppb Pt). (Tarkian et al., 2003).

Both chloride and bisulfide can form complexes with Pd and Pt in hydrothermal fluids under different conditions (Wood, 1987; Barnes and Liu, 2012), and experimental data suggest that hot, saline magmatic-hydrothermal fluids can transport PGE with chloride complexes. At temperatures above 500 °C where neutral species and hypersaline solutions are expected to be dominant, the PGE are soluble as chloride complexes in the liquid phase (Wood, 1987; Gammons, 1996; Hanley et al., 2005); such early-stage magmatic-hydrothermal fluids are estimated to be able to dissolve at least 10 ppb Pd (Xiong and Wood, 2000). On the other hand, unusual conditions are needed for PGE to be soluble as chloride complexes at low temperatures; these can include hydrothermal fluids with high oxidation states (at the Mn_3O_4-Mn_2O_3 buffer), high salinities and low pH (Gammons et al., 1992; Xiong and Wood, 2000). These conditions are not typical for porphyry-skarn Cu systems. Thermodynamic modelling suggests that a sulfur-bearing fluid can dissolve Pd and Pt at low temperatures (300 °C) as bisulfide complexes (Barnes and Liu, 2012), but such a mechanism is not applicable to carbonate host rock scenarios due to their ability to buffer the pH. The fluid inclusion results for Cp-Py and Py-Cp-Sph assemblages at Jiguanzui-Taohuazui (400–250 °C, 300–220 °C, respectively) suggest that they are within the right temperature range (Zhang, 2015), but it unlikely the mineralizing fluids were highly acidic as they would have been neutralized by the interactions with the limestone host rock.

Our data show that the early-stage Mt-Bn-Cp-Hm assemblage precipitating from the high temperature (530–380 °C) and high salinity

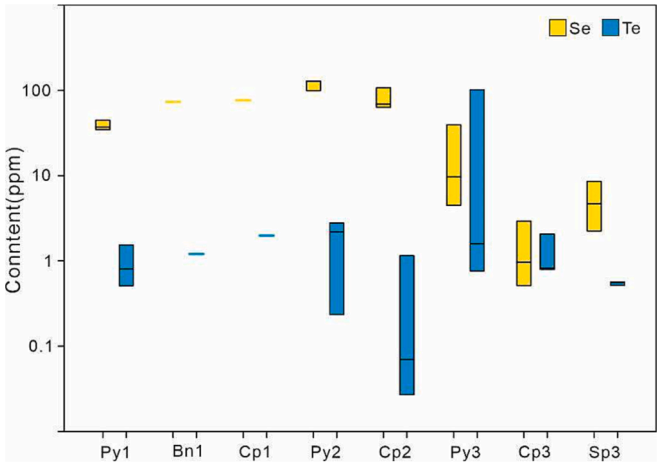

Fig. 9. Box diagram of Te and Se concentrations for the Jiguanzui-Taohuazui sulfides. Bn-bornite; Cp-chalcopyrite; Py-pyrite. The number 1, 2, and 3 represents the Mt-Bn-Cp-Hm assemblage, the Cp-Py assemblage, and the Py-Cp-Sph assemblage, respectively.

Table 5
Trace element data for sulfide minerals from the Jiguanzui-Taohuazui deposit.

Sample	Mineral	^{59}Co	^{60}Ni	^{75}As	^{77}Se	^{95}Mo	^{107}Ag	^{125}Te	^{197}Au	^{208}Pb	^{209}Bi	Mineral assemblage
JZ100-py-1	pyrite	16501.2	16.7	107.1	44.8	b.d.	b.d.	b.d.	b.d.	b.d.	b.d.	Mt-Bn-Cp-Hm
JZ100-py-2	pyrite	10788.8	13.9	94.0	34.8	b.d.	b.d.	b.d.	b.d.	0.3	1.2	Mt-Bn-Cp-Hm
JZ100-py-3	pyrite	8341.0	15.5	82.5	37.3	b.d.	b.d.	b.d.	b.d.	b.d.	b.d.	Mt-Bn-Cp-Hm
JZ100-bn-1	bornite	b.d.	b.d.	b.d.	45.4	0.1	883.1	b.d.	0.0	1.1	32.8	Mt-Bn-Cp-Hm
JZ100-bn-2	bornite	0.1	0.6	1.0	101.7	0.1	920.7	b.d.	0.0	5.2	38.3	Mt-Bn-Cp-Hm
JZ100-cp-1	chalcopyrite	b.d.	1.4	b.d.	55.1	b.d.	40.2	b.d.	0.0	13.6	6.1	Mt-Bn-Cp-Hm
JZ100-cp-2	chalcopyrite	0.1	b.d.	b.d.	98.6	b.d.	74.6	2.9	b.d.	13.4	11.1	Mt-Bn-Cp-Hm
JZ88-py-1	pyrite	2.0	25.7	5.5	127.8	b.d.	0.3	2.8	0.1	0.9	7.8	Cp-Py
JZ88-py-2	pyrite	0.2	0.7	0.4	129.4	b.d.	0.6	0.2	0.1	3.0	9.4	Cp-Py
JZ88-py-3	pyrite	3.5	1.5	0.6	99.4	0.0	0.4	2.2	0.1	1.2	10.1	Cp-Py
JZ88-cp-1	chalcopyrite	b.d.	b.d.	7.1	69.3	5.0	1.8	b.d.	0.1	11.1	15.5	Cp-Py
JZ88-cp-2	chalcopyrite	0.0	0.3	0.9	107.6	0.8	2.8	1.2	0.1	1.7	7.1	Cp-Py
JZ88-cp-3	chalcopyrite	0.1	1.3	b.d.	63.5	1.0	3.5	b.d.	b.d.	3.7	23.2	Cp-Py
JZ218-py-1	pyrite	9.9	0.4	18.0	49.3	b.d.	b.d.	39.3	b.d.	b.d.	b.d.	Py-Cp-Sph
JZ218-py-2	pyrite	0.0	b.d.	72.4	3.2	b.d.	b.d.	101.8	b.d.	b.d.	0.0	Py-Cp-Sph
JZ218-py-3	pyrite	9.7	b.d.	84.3	13.7	b.d.	b.d.	175.4	b.d.	b.d.	0.0	Py-Cp-Sph
JZ94-py-1	pyrite	0.5	0.8	135.4	b.d.	0.0	0.2	b.d.	b.d.	0.3	b.d.	Py-Cp-Sph
JZ94-py-2	pyrite	0.6	1.7	36.3	5.8	b.d.	b.d.	b.d.	b.d.	0.2	b.d.	Py-Cp-Sph
JZ94-py-3	pyrite	0.6	1.4	148.7	9.7	b.d.	b.d.	0.7	b.d.	2.8	b.d.	Py-Cp-Sph
JZ94-cp-1	chalcopyrite	0.1	b.d.	10.2	2.9	b.d.	6.4	2.1	0.0	1.5	1.2	Py-Cp-Sph
JZ94-cp-2	chalcopyrite	6.7	6.5	665.9	b.d.	b.d.	10.0	b.d.	0.1	93.5	17.7	Py-Cp-Sph
JZ94-cp-3	chalcopyrite	1.6	b.d.	48.0	b.d.	b.d.	11.4	b.d.	0.2	29.0	3.0	Py-Cp-Sph
JZ94-sph-1	sphalerite	0.2	0.6	5.7	b.d.	1.5	4.5	b.d.	b.d.	15.6	2.9	Py-Cp-Sph
JZ94-sph-2	sphalerite	0.0	b.d.	1.3	4.7	0.1	2.7	b.d.	b.d.	2.4	0.6	Py-Cp-Sph
JZ94-sph-3	sphalerite	0.0	b.d.	1.1	8.6	0.2	2.6	b.d.	b.d.	8.5	2.7	Py-Cp-Sph

fluids has a relatively higher Pd-Cu correlation ($r_{Mt\text{-}Bn\text{-}Cp\text{-}Hm} = 0.68$; Table 1). Both the Cp-Py and Py-Cp-Sph assemblages at Jiguanzui-Taohuazui, formed during late-stage lower temperature (400–250 °C and 300–220 °C, respectively) mineralization, seem to deviate from this trend ($r_{Cp\text{-}Py} = 0.00$; $r_{Py\text{-}Cp\text{-}Sph} = 0.35$, Table 1, Fig. 6). Petrographic studies of the "High Cu low Pd" samples shows that four of the six samples contain "fingerprint pyrite" (Fig. 4d l). Such textures are indicative of supersaturation caused by a rapid change in physico-chemical environment such as fluid mixing (Roedder, 1968; Maslennikov et al., 2009). The drop of temperature and salinity documented in this assemblage indicates the input of significant quantity of external water, and coexisting marcasite (Fig. 4l) in these samples supports relative low temperatures (typically lower than 240 °C) and an neutral to acid environment (Hannington and Scott, 1985). This may be the result of the sudden change from lithostatic pressures to hydrostatic pressures in the system and the ingress of meteoric waters. As our results show that PGE at Jiguanzui-Taohuazui are not hosted in Cu-bearing sulfides, the positive Pd-Cu correlation in the early-stage Mt-Bn-Cp-Hm assemblage may be caused by the temperature control on both PGE and Cu solubilities, and the later lower temperature stage Cu saturation can be caused by multi factors such as sudden pressure changes and fluid mixing. Previous studies have reported high Pd contents (up to 1806 ppb) in Fe-Cu skarn ores with significant magnetite mineralization e.g., in the Tonglushan deposit (Gu and Chen, 1993). Here we document that the primary PGE tenor is found in the Cu-Au concentrates, while the Fe concentrates are poor sources of PGE (Fig. 7). This may imply that although the major PGE mineralization occurs in sulfides in the high temperature magnetite stages, but that magnetite itself is not the main host. Therefore, we suggest that the declining magmatic-hydrothermal fluid temperature and salinity in the early Mt-Bn-Cp-Hm stages can lead to PGE precipitation in sulfides, whereas fluid mixing in the later stages of the hydrothermal system does not.

6.2. Distribution and hydrothermal transport of Se and Te

Selenium and Te in rocks are typically found as (1) independent stoichiometric minerals and (2) as substitutions for S in the lattices of sulfide minerals (Keith et al., 2018). Selenide minerals are seldom reported in high temperature mineralization rather, the Se tends to be incorporated into sulfide minerals (Maslennikov et al., 2009; Revan et al., 2014), although PGE selenide minerals occur in carbonate rocks at Jinchuan (Prichard et al., 2013); tellurides are more frequently reported than selenides in porphyry-skarn deposits, and they usually occur in late epithermal-stage mineralization (Afifi et al., 1988; Han et al., 2019; Voudouris et al., 2022). The positive correlations in Se vs S and Te vs S shown in this study imply that S precipitation may be a trigger for Se and Te mineralization during the hydrothermal process (Fig. 6h i).

The most dominant Se-bearing mineralization is developed within the Py-Cp-Sph assemblage in marble (Fig. 5c; Fig. 6i). The precipitation of Se may result from (i) changes of f_{Se2}/f_{S2} ratio (Simon et al., 1997), (ii) Se-S substitution in sulfide minerals (Keith et al., 2018), or (iii) carbonate neutralization where Bi-bearing platinum group minerals occur (Prichard et al., 2013). There are minor Se contents in Bi-Te-S minerals identified in this study according to the EPMA data (~0.6 wt%, Table 3), however, the three assemblages show generally higher bulk ore Se concentrations than that of Te (Fig. 5c d; Fig. 6g). The abundant bismuth tellurides and rare selenides at Jiguanzui-Taohuazui, and the relatively high Se contents and low Te contents in sulfide minerals (Fig. 9) jointly demonstrate that major Se is incorporated into sulfide minerals at Jiguanzui-Taohuazui, as case (ii) suggested. The LA-ICP-MS data indicate that sulfides from the Mt-Bn-Cp-Hm and the Cp-Py have higher Se contents than sulfides from the Py-Cp-Sph assemblage, and that all the sulfides from the Py-Cp-Sph assemblage (pyrite, chalcopyrite and sphalerite) have low Se concentrations (Fig. 9). This is consistent with the low Se/S ratios of the Py-Cp-Sph assemblage in the bulk ore analyses (Fig. 5e). As Se is mainly incorporated into sulfide minerals, despite the low Se concentrations in the sulfide minerals, the elevated bulk ore Se contents are in the sulfide rich Py-Cp-Sph assemblage ore (Fig. 5c; Fig. 6i).

Similarly, the analytical results in this study demonstrate that the major Te mineralization occurs in the low temperature Py-Cp-Sph assemblage of marble-replacement ore, and is associated with major sulfide deposition (Fig. 5d). The abundant Bi-Te-S minerals at Jiguanzui-Taohuazui (Fig. 8) and the low Te contents in sulfide minerals (Fig. 9) indicate that independent Te-bearing minerals are the major Te-bearing phases. Tellurium-S cross plots reveal a positive correlation between the Te and S contents in the bulk ore (Fig. 6h). Thermodynamic calculations and experimental studies suggest that alkaline and oxidized magmatic fluids are capable of transporting Te(IV) complexes in the liquid phase, and a lower pH and reduction of such fluids may lead to $Te_2(g)$ vapor transport (Fig. 10a b; Grundler et al., 2013; Zhai et al., 2018). The shift from the magnetite-hematite buffer in the Mt-Bn-Cp-Hm stage to the pyrite stability areas in the Py-Cp-Sph stage suggest a declining redox state, and the coexisting marcasite implies a slight change in pH in the Py-Cp-Sph stage (Hannington and Scott, 1985). These changes in the chemical parameters of the fluid can lead to a decline of Te solubility in the liquid phase (Fig. 10a). The evidence for fluid boiling in the Cp-Py and Py-Cp-Sph stages (Zhang, 2015) supports a model whereby Te is partitioned from the liquid into the vapor phase (Fig. 10c), leading to an elevation of f_{Te2}. Ultimately, the major precipitation of sulfide minerals (observed in hand specimens and evidenced by their elevated S contents) in the Py-Cp-Sph assemblage leads to a dramatic decrease in f_{S2}, and the increasing f_{Te2}/f_{S2} ratio (Fig. 11) causes the major Te mineralization (deposition of Bi-Te-S minerals) at Jiguanzui-Taohuazui, a process proposed by Afifi et al., (1988).

The mechanism by which Te is incorporated into sulfide is debated, and different studies have suggested different incorporation mechanisms (Huston et al., 1995; Butler and Nesbitt, 1999; Keith et al., 2018; Martin et al., 2019). Butler and Nesbitt (1999) hold that as Te^{2-} is 16 % larger than S^{2-}, the Te-S substitution in the mineral lattice will be favored by high temperatures, whereas Keith et al (2018) suggest Te is incorporated as micro- to nano-scale inclusions in sulfide minerals due to the non-negligible difference of their covalent radii. The Te concentrations normalized by the S contents of the ore from the Jiguanzui-Taohuazui deposit show no significant variations in the three assemblages (Fig. 5f). The three abnormally high Te contents in pyrite return from the sample JZ218 from the Py-Cp-Sph assemblage (Table 5), and this sample hosts abundant Bi-Te-S minerals. However, Bi contents of the three analyses are near, or below, the detection limits (Table 5), excluding the possibility of Bi-Te mineral inclusions; therefore, it is likely that Te is in the pyrite lattice in this sample. The Se and Te enrichment is found in copper–gold concentrates and not in the Fe concentrates which suggests that magnetite is not a host for either element (Fig. 7).

6.3. Comparison of Pd–Pt–Se–Te enrichment of Cu-Au and Cu-Mo deposits

To compare the differences of Pd, Pt, Se and Te enrichment in porphyry-skarn Cu-Au and Cu-Mo deposits, a plot of the Pd, Pt, Se, and Te vs Cu concentrations of ore samples from the Jiguanzui-Taohuazui (representative Cu-Au) and Tongshankou (representative Cu-Mo) deposits in the Edong ore district are shown in Fig. 12. The PGE rich Mt-Bn-Cp-Hm assemblage ores from Jiguanzui-Taohuazui generally show higher Pd ranges than Cu-Mo ores from Tongshankou, but have comparable Pt ranges (Fig. 12a b). The ore from Jiguanzui-Taohuazui has a higher range of Te concentrations, whereas the bulk ore Se concentrations from the two deposits generally overlap (Fig. 12c d). Given the similar timing and tectonic settings at Jiguanzui-Taohuazui and Tongshankou, this may suggest that porphyry-skarn Cu-Au deposit have more potential for PGE and Te mineralization than the Cu-Mo deposit. Globally, John and Taylor (2016) plotted the amounts of PGE (Pd + Pt) in 40

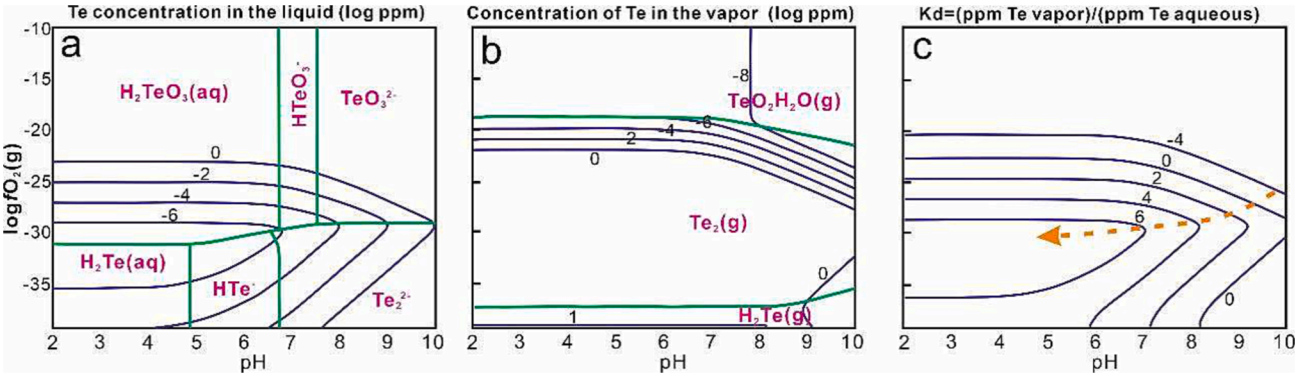

Fig. 10. Speciation and solubility of Te in the brine (a) and vapor (b) for the system Au–Te–H_2O–S–Cl at 300 °C at vapor saturation pressures (modified from Grundler et al., 2013). The process of boiling and the declined pH may lead to vapor transport of Te (c).

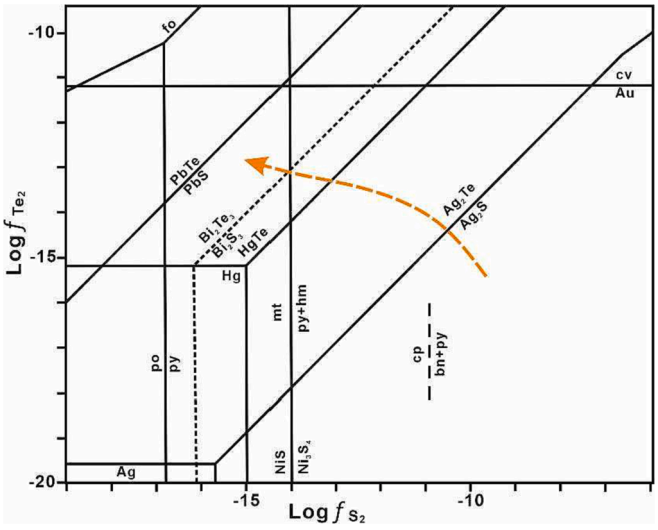

Fig. 11. Log f_{S2} versus log f_{Te2} diagrams showing the fields of stability for sulfides and tellurides at 200 °C at vapor saturation (modified after Afifi et al., 1988). The arrow indicates the increased f_{Te2} caused by fluid boiling and liquid acidity increasing, and the declined f_{S2} led by major sulfide deposition. Abbreviations: cp-chalcopyrite; cv-calaverite; bn-bornite; fo-frohbergite; hm-hematite; mt-magnetite; po-pyrrhotite; py-pyrite.

(oxidized) porphyry Cu and Mo deposits as a grade-tonnage plot. Our modification to separate Cu-Mo and Cu-Au deposits from Cu deposits shows generally lower PGE contents for porphyry Mo and Cu-Mo deposits and higher contents in Cu-Au and Cu deposits, with averaging Pd + Pt grades of 0.6 ppb, 2.4 ppb, 9.6 ppb and 20.8 ppb for Mo, Cu-Mo, Cu and Cu-Au deposits, respectively (Fig. 13a). Plots of bulk ore results from previous case studies of porphyry (±skarn) Cu-Au and Cu-Mo deposits are shown in Fig. 13b c d e. As the porphyries associated with skarn usually show higher ore grades than those which do not develop skarn alteration (Einaudi, 1982), we use (Pd + Pt) vs S (Fig. 13b), Te vs S (Fig. 13c) and Se vs S (Fig. 13d) diagrams to normalize the intensity of sulfide mineralization (S content). The results generally show higher bulk ore PGE and Te concentrations in the Cu-Au deposits than in Cu-Mo deposits at the same S contents (Fig. 13b c), and have overlapping Se concentrations at the same S contents for both deposit types (Fig. 13d e). The Cu-Au deposits show higher ranges of Te contents than the Cu-Mo deposits, but similar Se ranges (Fig. 13e). This result is consistent with the plenty of reports of tellurides occurring in the Au-rich porphyry and skarn deposits (Kalmakyr, Pašava et al. 2010; Big Gossan, Prendergast et al., 2005; Skouries, McFall et al., 2018). This suggests that porphyry (±skarn) Cu-Au deposits have more potential to be PGE and Te enriched than the Cu-Mo deposits, and therefore, may be the better target for PGE and Te recovery.

Previous studies have proposed that the segregation of magmatic sulfide will result in strong partition of highly siderophile Au into the S phase from the silicate melt (Campbell and Naldrett, 1979; Peach et al., 1990; Wilkinson, 2013). Since the PGE and Te also have high partition coefficients between the magmatic sulfide and silicate melt ($D^{sul/sil}$; ~5 × 10^5 for Pd, ~3 × 10^5 for Pt, 1005–10,000 for Te), their geochemical behavior during this process greatly resembles that of Au ($D^{sul/sil}$ = 11,200), and even minor amounts of sulfide cumulates may deplete these elements from the parental magma (Richards, 2009; Patten et al., 2013; Mungall and Brenan, 2014; Holwell et al., 2019). The $D^{sul/sil}$ of Se and Cu are much lower than the above-mentioned elements in the relatively oxidized magmas for typical porphyry and skarn Cu deposits (~20 to ~ 200 for Se, 1334 ± 210 for Cu, Li et al., 2021; Patten et al., 2013), therefore, they will not be significantly depleted with small amounts of magmatic sulfide precipitation.

Several previous studies have suggested that the tectonic setting may control the PGE fertility of porphyry (±skarn) Cu deposits (Economou-Eliopoulos et al., 2017; Wang et al., 2020). However, this has been challenged by a recent, global, data comparison study (McFall et al., 2021), which suggested both subduction-related and post-subduction deposits can be PGE, Te and Se enriched. It has been suggested that the high oxidation state of subduction-related magmas may prevent formation of magmatic sulfides (Mungall et al., 2006), however, such highly oxidized arc magmas (ΔFMQ + 2) are rare, which makes it difficult to suppress the sulfide phases (Richards, 2009; Lee et al., 2012). The magmatic sulfide hosting siderophile and chalcophile elements stripped from the silicate melt may accumulate in the lower crust, trapping these elements. Under ideal conditions (the 'Goldilocks' temperature of ~1100–1200 °C) during post-subduction stages, incongruent sulfide melting can selectively mobilize the Cu-rich sulfide (hosting siderophile and chalcophile elements) upwards through the crust, leaving the Ni-Fe rich sulfides at depth (Holwell et al., 2022). Since both the metasomatized mantle wedge and the cumulate residue sulfides are considered to be possible sources of Au, PGE, Se and Te (Richards, 2009; Jenner, 2017), the evolution of the magma chamber may be a governing factor in Pd–Pt–Se–Te enrichment in later magmatic-hydrothermal processes.

Typically, because of the exponential increase of sulfur contents at sulfide saturation (SCSS) with decreasing pressure, the ascending magmas tend to be undersaturated in sulfur (Mavrogenes and O'Neill, 1999; Holwell et al., 2019), but addition of S and/or reducing materials, such as assimilation of S-rich and/or reducing sediments can lead to the formation of sulfides in the magmatic process (Lesher and Burnham, 2001; Ripley and Li, 2003; Wilkinson, 2013). It has been suggested that the magmas that generate porphyry Mo and Cu-Mo deposits may have experienced more crustal contamination, with Mo being sourced from

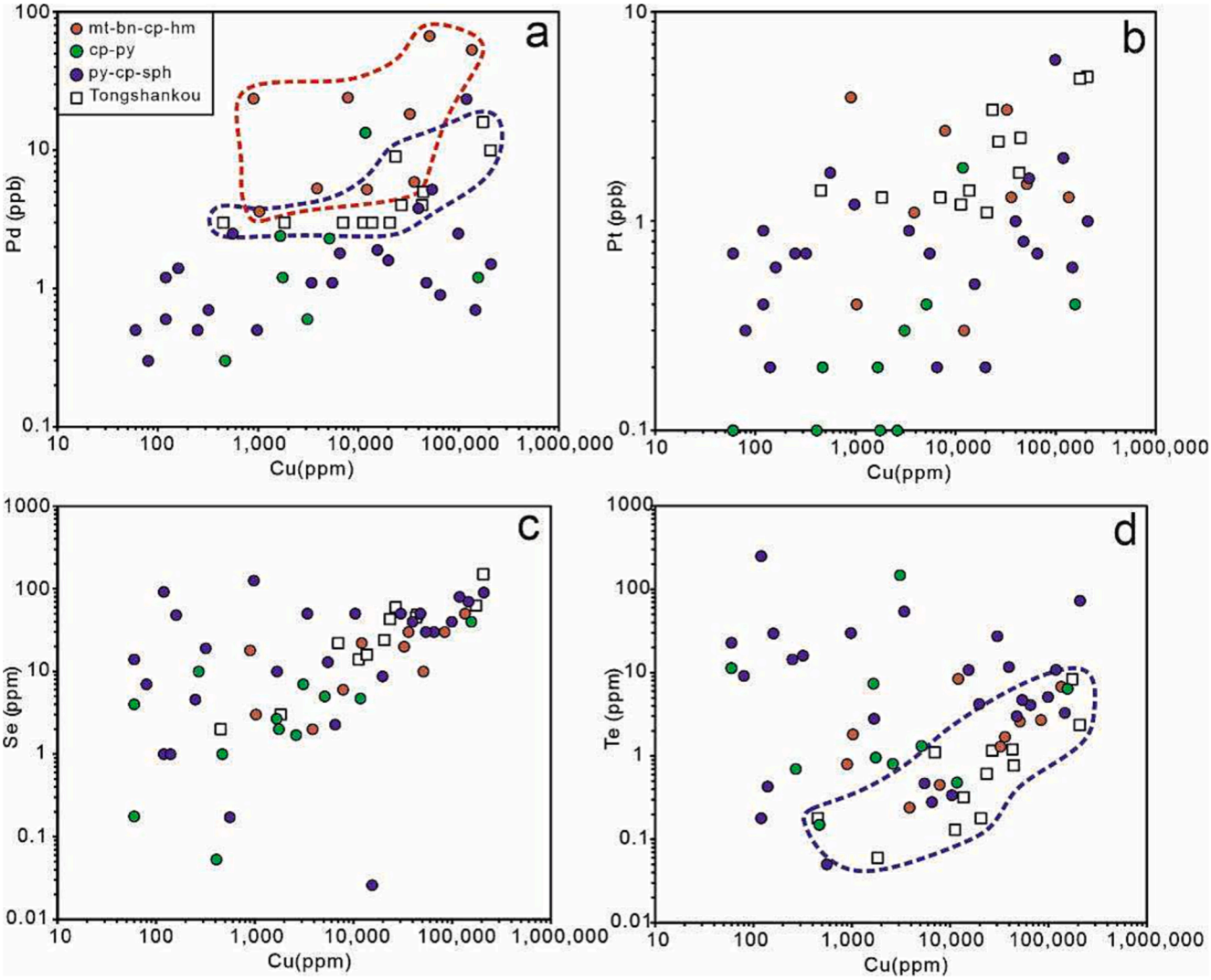

Fig. 12. Diagrams of Pd, Pt, Se, Te and Cu contents of samples from representative porphyry-skarn Cu-Au (Jiguanzui-Taohuazui) and Cu-Mo (Tongshankou) deposits in the Edong ore district. (a) the PGE rich Mt-Bn-Cp-Hm assemblage in the Jiguanzui-Taohuazui Cu-Au deposit has higher Pd values than the PGE rich ore from the Tongshankou Cu-Mo deposit; (b) the PGE rich Mt-Bn-Cp-Hm assemblage in the Jiguanzui-Taohuazui deposit has similar Pt ranges compared with the PGE rich ore from the Tongshankou Cu-Mo deposit; (c) the range of Se concentrations in ore from the two deposits largely overlap; (d) ore of the Jiguanzui-Taohuazui deposit have significantly higher Te concentrations than that of the Tongshankou deposit. Data from the Tongshankou deposit are from Wang et al. (2020).

the continental crust (Farmer and DePaolo, 1984; Stein, 1988; Klemm et al., 2008). Considering the low abundances of Pd, Pt, Se, and Te in the crust, a greater proportion of contamination by crustal material will not supply these metals; adding sulfur and/or reducing materials to the magma will facilitate magmatic sulfide precipitation, which partitions Au, PGE and Te from the silicate melts (Fig. 14; Tarkian and Stribrny, 1999; Wilkinson, 2013; Mansur et al., 2020). This is consistent with our interpretation that porphyry (±skarn) Cu-Mo deposits are less enriched in Au, Pd, and Te than the Cu-Au deposits in the Edong ore district and elsewhere, however the Se contents are broadly similar. The comparable Pt ranges in the two types of the deposits (Fig. 12b) can be explained by the crystallization of Pt-bearing alloys during early source magma fractionation process (Park et al., 2013), stripping Pt early from the both systems, which also results in the predominance of Pd over Pt in porphyry Cu deposits. The $D^{sul/sil}$ value controls the coupled enrichment of Au, Pd, and Te in porphyry (±skarn) Cu-Au deposits, and the same grade ranges of Se between porphyry (±skarn) Cu-Au and Cu-Mo deposits demonstrate that the enrichment of PGE and Te is controlled by the assimilation of S-rich and/or reducing materials in the crust during magmatic evolution. Therefore, we propose that the proportion of crustal contamination during the magmatic process, which is an important factor for magmatic sulfide precipitation, governs the PGE and Te enrichment and too much crustal contamination can be detrimental to PGE and Te enrichment in porphyry (±skarn) Cu deposits.

7. Conclusions

(1) In the Jiguanzui-Taohuazui porphyry-skarn deposit, the major phase of PGE enrichment developed in the Mt-Bn-Cp-Hm assemblage ores which formed at temperatures between 530 and 380 °C. Major Se and Te mineralization occurs in a lower temperature (300–220 °C) ore assemblage of Py-Cp-Sph which replaced marble in the host rock. Palladium, Pt, and Se are mainly hosted in sulfide minerals, and Te is hosted as tellurides and sulfosalt minerals. Therefore, early high temperature magmatic-hydrothermal fluids can transport Pd and Pt in magmatic-hydrothermal systems, and the precipitation of major sulfide minerals (pyrite, chalcopyrite, and sphalerite) triggers Se and Te mineralization.

(2) A comparison between the porphyry (±skarn) Cu-Au and Cu-Mo deposits in the studied region (Edong) and global deposits suggests that Pd and Te are more enriched in Cu-Au deposits than in Cu-Mo deposits. This suggests that the degree of S-rich and/or reducing crustal

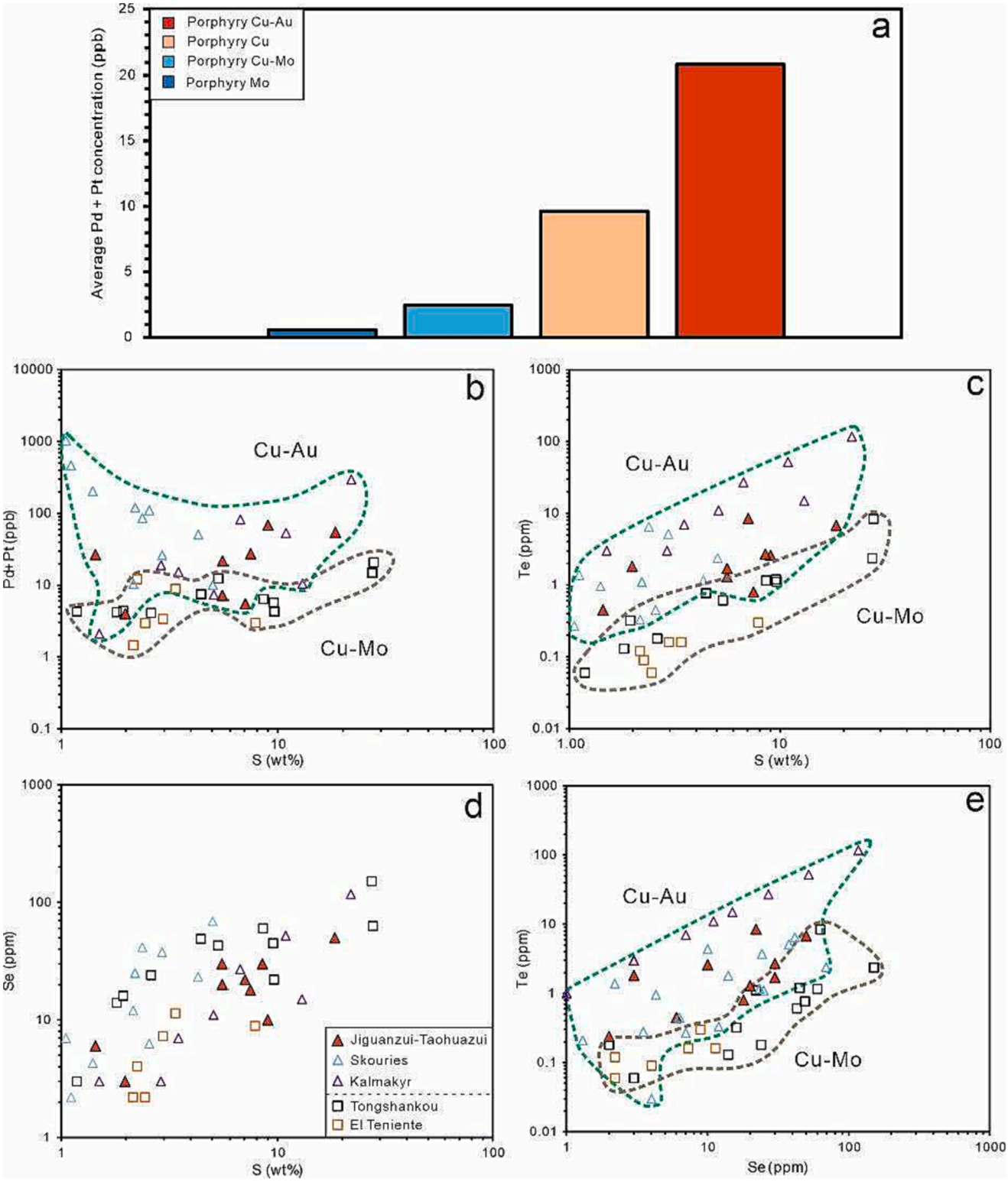

Fig. 13. Diagrams of average Pd + Pt values of 40 world porphyry Mo (3), Cu-Mo (7), Cu (18), and Cu-Au (12) deposits (a), (Pd + Pt) vs S (b), Te vs S (c), Se vs S (d), and Te vs Se (e) for selected porphyry (skarn) Cu-Au and Cu-Mo deposits, plotted with the PGE rich Mt-Bn-Cp-Hm assemblage in the Jiguanzui-Taohuazui deposit. Data sources: John and Taylor (2016) for average Pd + Pt grades of 40 world porphyry deposits; Eliopoulos and Economou-Eliopoulos (1991) and McFall et al. (2021) for Skouries; Pašava et al. (2010) for Kalmakyr; McFall et al. (2021) for El Teniente.

contamination, which affects the saturation of reduced sulfur in the magmatic process, could be governing factor of PGE and Te fertilization in porphyry Cu deposits.

Declaration of Competing Interest

The authors declare that they have no known competing financial interests or personal relationships that could have appeared to influence the work reported in this paper.

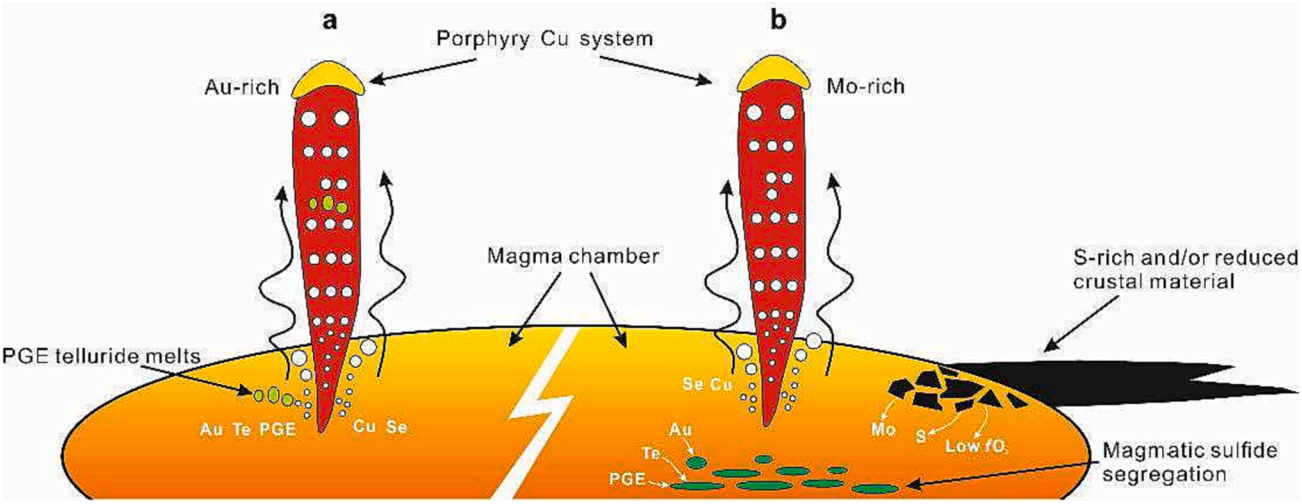

Fig. 14. Crustal contamination can introduce Mo, S, and lower Eh to the silicate melts in the magma chamber, facilitating saturation of magmatic sulfide and partition of Au, PGE, and Te from the parental magma. This model is inspired by Wilkinson (2013) and Holwell et al. (2019).

Data availability

Data will be made available on request.

Acknowledgments

This work is financially supported by the National Science Foundation of China (92162217 and 41925011). We would like to acknowledge Xiaoyu Shang and Yunhao Ji for collaborative fieldwork efforts. We express our appreciation to Prof. Zhenyu Chen, Dr. Xiaodan Chen, and Dr. Zhen Wang for their assistance in the electron microprobe analysis. We thank Hubei Sanxin Gold & Copper Co., Ltd and the First Geological Brigade of Hubei Geological Bureau for their kind support in the fieldwork for this study. Sarah A. Gleeson is supported by a Helmholtz Recruitment Initiative. This manuscript benefited significantly from constructive and extensive comments from Dr. Iain McDonald and three anonymous reviewers.

Appendix A. Supplementary data

Supplementary data to this article can be found online at https://doi.org/10.1016/j.oregeorev.2023.105335.

References

Afifi, A.M., Kelly, W.C., Essene, E.J., 1988. Phase relations among tellurides, sulfides, and oxides: II, applications to telluride–bearing ore deposits. Econ. Geol. 83, 395–404.
Barnes, S.J., Liu, W.H., 2012. Pt and Pd mobility in hydrothermal fluids: evidence from komatiites and from thermodynamic modelling. Ore Geol. Rev. 44, 49–58.
Butler, I.B., Nesbitt, R.W., 1999. Trace element distributions in the chalcopyrite wall of a black smoker chimney: insights from laser ablation inductively coupled plasma mass spectrometry (LA–ICP–MS). Earth Planet. Sci. Lett. 167, 335–345.
Campbell, I.H., Naldrett, A.J., 1979. The influence of silicate: sulfide ratios on the geochemistry of magmatic sulfides. Econ. Geol. 74, 1503–1506.
Chang, Y.F., Liu, X.P., Wu, C.Y., 1991. The copper–iron belt of the Lower and Middle reaches of the Changjiang River. In: Geological Publishing House, pp. 1–234 in Chinese with English abstract.
Danyushevsky, L., Robinson, P., Gilbert, S., Norman, M., Large, R., McGoldrick, P., Shelley, M., 2011. Routine quantitative multi-element analysis of sulphide minerals by laser ablation ICP-MS: Standard development and consideration of matrix effects. Geochem.-Explor. Environ. Anal. 11 (1), 51–60.
Duan, D.F., Jiang, S.Y., 2018. Using apatite to discriminate synchronous ore-associated and barren granitoid rocks: a case study from the Edong metallogenic district, South China. Lithos 310–311, 369–380.
Economou-Eliopoulos, M., 2005. Platinum-group element potential of porphyry deposits. In: Mungall, J. (Ed.), Exploration for Deposits of Platinum-Group Elements. Mineralogical Association of Canada, Oulu, Finland, pp. 203–246.
Economou-Eliopoulos, M., Eliopoulos, D.G., Tsoupas, G., 2017. On the diversity of the PGE content in chromitites hosted in ophiolites and in porphyry-Cu systems: Controlling factors. Ore Geol. Rev. 88, 156–173.
Einaudi, M.T., 1982. General features and origin of skarns associated with porphyry copper plutons, Southwestern North America. In: Titley, S.R. (Ed.), Advances in Geology of the Porphyry Copper Deposits, Southwestern North America. University of Arizona Press, pp. 185–210.
Eliopoulos, D.G., Economou-Eliopoulos, M., 1991. Platinum-group element and gold contents in the Skouries porphyry copper deposit, Chalkidiki Peninsula, Northern Greece. Econ Geol. 86, 740–749.
Eliopoulos, D.G., Economou-Eliopoulos, M., Zelyaskova-Panayiotova, M., 2014. Critical factors controlling Pd and Pt potential in porphyry Cu–Au deposits: evidence from the Balkan Peninsula. Geosciences 4, 31–49.
Farmer, G.L., DePaolo, D.J., 1984. Origin of Mesozoic and Tertiary granite in the western United States and implications for pre-Mesozoic crustal structure, 2. Nd and Sr isotopic studies of unmineralized and Cu- and Mo-mineralized granite in the Precambrian craton. J. Geophys. Res. 89, 10141–10160.
Gammons, C.H., 1996. Experimental investigations of the hydrothermal geochemistry of platinum and palladium: V. Equilibria between platinum metal, Pt(II), and Pt(IV) chloride complexes at 25 to 300 °C. Geochim. Cosmochim. Acta 60, 1683–1694.
Gammons, C.H., Bloom, M.S., Yu, Y., 1992. Experimental investigation of the hydrothermal geochemistry of platinum and palladium: I. Solubility of platinum and palladium sulphide minerals in NaCl/H2SO4 solutions at 300 °C. Geochim. Cosmochim. Acta 56, 3881–3894.
Geological Team of Southeast Hubei Province, 1988. Geological survey report of Jiguanzui Cu-Au mining area, Daye County, Hubei Province.1-203. (in Chinese).
Gilbert, S., Danyushevsky, L., Robinson, P., Wohlgemuth-Ueberwasser, C., Pearson, N., Savard, D., Norman, M., Hanley, J., 2013. A comparative study of five reference materials and the Lombard meteorite for the determination of the platinum-group elements and gold by LA-ICP-MS. Geostand. Geoanal. Res. 37 (1), 51–64.
Grundler, P.V., Brugger, J., Etschmann, B.E., Helm, L., Liu, W., Spry, P.G., Tian, Y., Testemale, D., Pring, A., 2013. Speciation of aqueous tellurium (IV) in hydrothermal solutions and vapors, and the role of oxidized tellurium species in Te transport and gold deposition. Geochim. Cosmochim. Acta 120, 298–325.
Gu, X.P., Chen, D.S., 1993. Palladium and platinum in some copper (iron) deposits of skarn type and related ore processing and smelting products in China. Mineral Resour. Geol. 7, 282–285 in Chinese with English abstract.
Gunn, G., 2014. Critical Metals Handbook. Wiley, New York, pp. 1–439.
Han, Y.X., Mao, J.W., Xie, G.Q., Lehmann, B., 2019. Linkage of distal vein–type Au mineralization in carbonate rocks with Cu–Au skarn mineralization in the Fengshan area, Eastern China: mineralogy and stable isotope geochemistry. Ore Geol. Rev. 119, 1–20.
Hanley, J.J., Pettke, T., Mungall, J.E., Spooner, E.T.C., 2005. The solubility of platinum and gold in NaCl brines at 1.5 kbar, 600 to 800 °C: a laser ablation ICP-MS pilot study of synthetic fluid inclusions. Geochim. Cosmochim. Acta 69, 2593–2611.
Hannington, M., Scott, S., 1985. A Caldera-hosted Silica-sulfate-sulfide Deposit, Axial Seamount, Central Juan de Fuca Ridge, N.E. Pacific Ocean [abstr.].
Holwell, D.A., Fiorentini, M.L., Knott, T.R., McDonald, I., Blanks, D.E., McCuaig, T.C., Gorczyk, W., 2022. Mobilisation of deep crustal sulfide melts as a first order control on upper lithospheric metallogeny. Nat. Commun. 13, 573.
Holwell, D.A., Fiorentini, M., McDonald, I., Lu, Y., Giuliani, A., Smith, D.J., Keith, M., Locmelis, M., 2019. A metasomatized lithospheric mantle control on the metallogenic signature of post-subduction magmatism. Nat. Commun. 10, 1–10.
Huston, D.L., Sie, S.H., Suter, G.F., Cooke, D.R., Both, R.A., 1995. Trace elements in sulfide minerals from eastern Australian volcanic-hosted massive sulfide deposits; Part I, Proton microprobe analyses of pyrite, chalcopyrite, and sphalerite, and Part II, Selenium levels in pyrite; comparison with delta 34 S values and implications for the source of sulfur in volcanogenic hydrothermal systems. Econ. Geol. 90, 1167–1196.
Jenner, F.E., 2017. Cumulate causes for the low contents of sulfide-loving elements in the continental crust. Nat. Geosci. 10, 524–529.

John, D.A., Taylor, R.D., 2016. By-products of porphyry copper and molybdenum deposits. Rev. Econ. Geol. 18, 137–164.
Jowitt, S.M., Mudd, G.M., Werner, T.T., Weng, Z.H., Barkoff, D.W., McCaffrey, D., 2018. The critical metals: an overview and opportunities and concerns for the future. Soc. Econ. Geologists Spec. Publ. 21, 25–38.
Ke, Y.F., Cai, H.G., Du, K., Wu, Y.X., Yuan, H.W., 2016. Analyses of geological characteristics and prospecting potential of Jiguanzui Cu-Au Deposits in Daye City, Hubei province. Resour. Environ. Eng. 30, 817–824 in Chinese with English abstract.
Keith, M., Smith, D.J., Jenkin, G.R.T., Holwell, D.A., Dye, M.D., 2018. A review of Te and Se systematics in hydrothermal pyrite from precious metal deposits: insights into oreforming processes. Ore Geol. Rev. 96, 269–282.
Kelley, K.D., Spry, P.G., 2016. Critical elements in alkaline igneous rock-related epithermal gold deposits. Rev. Econ. Geol. 18, 195–216.
Klemm, L.M., Pettke, T., Heinrich, C.A., 2008. Fluid and source magma evolution of the Questa porphyry Mo deposit, New Mexico, USA. Miner. Deposita 43, 533–552.
Kosler, J., 2001. Laser-ablation ICPMS study of metamorphic minerals and processes. In: Sylvester, P.J. (Ed.), Laser-Ablation-ICPMS in the Earth Sciences: Principles and Applications. Mineralogical Association of Canada Short Course Handbook, Ottawa, pp. 185–202.
Kouzmanov, K., Pettke, T., Heinrich, C.A., 2010. Direct analysis of ore-precipitating fluids: combined IR Microscopy and LA-ICP-MS Study of fluid inclusions in opaque ore minerals. Econ. Geol. 105, 351–373.
Lee, C.T.A., Luffi, P., Chin, E.J., Bouchet, R., Dasgupta, R., Morton, D.M., Roux, V.L., Yin, Q.Z., Jin, D., 2012. Copper systematics in arc magmas and implications for crust–mantle differentiation. Science 336, 64–68.
Lesher, C.M., Burnham, O.M., 2001. Multicomponent elemental and isotopic mixing in Ni–Cu–(PGE) ores at Kambalda, Western Australia. Can. Mineral 39, 421–446.
Li, J.W., Zhao, X.F., Zhou, M.F., Vasconcelos, P., Ma, C.Q., Deng, X.D., de Souza, Z.S., Zhao, Y.X., Wu, G., 2008. Origin of the Tongshankou porphyry-skarn Cu-Mo deposit, eastern Yangtze craton, Eastern China: geochronological, geochemical, and Sr-Nd-Hf isotopic constraints. Miner. Deposita 43, 315–336.
Li, J.W., Zhao, X.F., Zhou, M.F., Ma, C.Q., Souza de, Z.S., Vasconcelos, P., 2009. Late Mesozoic magmatism from the Daye region, eastern China: U-Pb ages, petrogenesis, and geodynamic implications. Contrib. Miner. Petrol. 157, 383–409.
Li, Y., Audétat, A., Liu, Z., Wang, F., 2021. Partitioning of V, Mn Co, Ni, Cu, Zn, As, Mo, Ag, Sn, Sb, W, Au, Pb, and Bi between sulfide phases and hydrous basanite melt at upper mantle conditions. Earth Planet. Sci. Lett. 355, 327–340.
Li, J.W., Vasconcelos, P.M., Zhou, M.F., Deng, X.D., Cohen, B., Bi, S.J., Zhao, X.F., Selby, D., 2014. Longevity of magmatic-hydrothermal systems in the Daye Cu-Fe-Au District, eastern China with implications for mineral exploration. Ore Geol. Rev. 57, 375–392.
Li, W., Xie, G.Q., Mao, J.W., Zhu, Q.Q., Zheng, J.H., 2019. Mineralogy, fluid inclusion, and stable isotope studies of the Chengchao deposit, Hubei province, eastern China: implications for the formation of high-grade Fe skarn deposits. Econ. Geol. 114, 325–352.
Lide, D.R., 2003. Handbook of Chemistry and Physics. CRC Press, Boca Raton, Florida.
Longerich, H.P., Jackson, S.E., Günther, D., 1996. Inter-laboratory note. Laser ablation inductively coupled plasma mass spectrometric transient signal data acquisition and analyte concentration calculation. J. Anal. At. Spectrom. 11 (9), 899–904.
Mansur, E.T., Barnes, S.J., Duran, C.J., 2020. An overview of chalcophile element contents of pyrrhotite, pentlandite, chalcopyrite, and pyrite from magmatic Ni-Cu-PGE sulfide deposits. Miner. Deposita 56, 179–204.
Mao, J.W., Wang, Y.T., Lehmann, B., Yu, J.J., Du, A.D., Mei, Y.X., Li, Y.F., Zang, W.S., Stein, H.J., Zhou, T.F., 2006. Molybdenite Re–Os and albite 40Ar/39Ar dating of Cu–Au–Mo and magnetite porphyry systems in the Changjiang valley and metallogenic implications. Ore Geol. Rev. 29, 307–324.
Mao, J.W., Xie, G.Q., Duan, C., Pirajno, F., Ishiyama, D., Chen, Y.C., 2011. A tectono–genetic model for porphyry–skarn–stratabound Cu–Au–Mo–Fe and magnetite–apatite deposits along the Middle-Lower Yangtze River Valley, Eastern China. Ore Geol. Rev. 43, 294–314.
Martin, A.J., McDonald, I., MacLeod, C.J., Prichard, H.M., McFall, K., 2018. Extreme enrichment of selenium in the Apliki Cyprus-type VMS deposit, Troodos, Cyprus. Mineral Mag 82, 697–724.
Martin, A.J., Keith, M., McDonald, I., Haase, K.M., McFall, K.A., Klemd, R., MacLeod, C., 2019. Trace element systematics and ore-forming processes in mafic VMS deposits: evidence from the Troodos ophiolite, Cyprus. Ore Geol. Rev. 106, 205–225.
Maslennikov, V.V., Maslennikova, S.P., Large, R.R., Danyushevsky, L.V., 2009. Study of trace element zonation in vent chimneys from the silurian yaman-kasy volcanic-hosted massive sulfide deposit (Southern Urals, Russia) using laser ablation-inductively coupled plasma mass spectrometry (LA-ICPMS). Econ. Geol. 104, 1111–1141.
Mavrogenes, J.A., O'Neill, H.S.C., 1999. The relative effects of pressure, temperature and oxygen fugacity on the solubility of sulfide in mafic magmas. Geochim. Cosmochim. Acta 63, 1173–1180.
McFall, K.A., Naden, J., Roberts, S., Baker, T., Spratt, J., McDonald, I., 2018. Platinum-group minerals in the Skouries Cu-Au (Pd, Pt, Te) porphyry deposit. Ore Geol. Rev. 99, 344–364.
McFall, K.A., McDonald, I., Wilkinson, J.J., 2021. Assessing the role of tectono-magmatic setting in the precious metal (Au, Ag, PGE) and critical metal (Te, Se, Bi) endowment of porphyry Cu deposits. SEG Special Publ.cations 24 (2), 277–295.
Mungall, J.E., Brenan, J.M., 2014. Partitioning of platinum-group elements and Au between sulfide liquid and basalt and the origins of mantle-crust fractionation of the chalcophile elements. Geochem. Cosmochim. Acta 125, 265–289.
Mungall, J.E., Hanley, J.J., Arndt, N.T., Debecdelievre, A., 2006. Evidence from meimechites and other low-degree mantle melts for redox controls on mantle-crust fractionation of platinum-group elements. Proc. Natl. Acad. Sci. 103 (34), 12695–12700.
Pan, Y., Dong, P., 1999. The Lower Changjiang (Yangzi/Yangtze River) metallogenic belt, East China: intrusion- and wall rock-hosted Cu–Fe–Au, Mo, Zn, Pb, Ag deposits. Ore Geol. Rev. 15, 177–242.
Park, J.W., Campbell, I.H., Arculus, R.J., 2013. Platinum-alloy and sulfur saturation in an arc-related basalt to rhyolite suite: evidence from the Pual Ridge lavas, the eastern Manus Basin. Geochim. Cosmochim. Acta 101, 76–95.
Pašava, J., Vymazalová, A., Košler, J., Koneev, R., Jukov, A., Khalmatov, R., 2010. Platinum-group elements in ores from the Kalmakyr porphyry Cu–Au–Mo deposit, Uzbekistan: bulk geochemical and laser ablation ICP-MS data. Miner. Deposita 45, 411–418.
Patten, C., Barnes, S.J., Mathez, E.A., Jenner, F.E., 2013. Partition coefficients of chalcophile elements between sulfide and silicate melts and the early crystallization history of sulfide liquid: LA-ICP-MS analysis of MORB sulfide droplets. Chem. Geol. 358, 170–188.
Peach, C.L., Mathez, E.A., Keays, R.R., 1990. Sulfide melt–silicate melt distribution coefficients for noble metals and other chalcophile elements as deduced from MORB: implications for partial melting. Geochim. Cosmochim. Acta 54, 3379–3389.
Prendergast, K., Clarke, G.W., Pearson, N.J., Harris, K., 2005. Genesis of pyrite–Au–As–Zn–Bi–Te zones associated with Cu–Au skarns: evidence from the Big Gossan and Wanagon gold deposits, Ertsberg District, Papua, Indonesia. Econ. Geol. 100, 1021–1050.
Prichard, H., Knight, R., Fisher, P., McDonald, I., Zhou, M.-F., Wang, C., 2013. Distribution of platinum-group elements in magmatic and altered ores in the Jinchuan intrusion, China: an example of selenium remobilization by postmagmatic fluids. Miner. Deposita 48, 767–786.
Revan, M.K., Genc, Y., Maslennikov, V.V., Maslennikov, S.P., Large, R.R., Danyushevsky, L.V., 2014. Mineralogy and trace-element geochemistry of sulfide minerals in hydrothermal chimneys from the Upper-Cretaceous VMS deposits of the Eastern Pontideorogenic belt (NE Turkey). Ore Geol. Rev. 63, 129–149.
Richards, J.P., 2009. Postsubduction porphyry Cu–Au and epithermal Au deposits: products of remelting of subduction-modified lithosphere. Geology 37, 247–250.
Ripley, E.M., Li, C., 2003. Sulfur isotope exchange and metal enrichment in the formation of magmatic Cu-Ni-(PGE) deposits. Econ. Geol. 98, 635–641.
Roedder, E., 1968. The non-colloidal origin of 'colloform' textures in sphalerite ores. Econ. Geol. 63 (5), 451–471.
Rudnick R.L., Gao S., 2003, The composition of the continental: Treatise on Geochemistry 3, 1–64.
Schulz K.J., DeYoung J.H., Bradley D.C., Seal R.R., 2017. II. Critical mineral resources of the United States—an introduction. In: Critical mineral resources of the United States—economic and environmental geology and prospects for future supply. Reston: U. S. Geological Survey A1–A14.
Shu, Q.A., Chen, P.L., Cheng, J.R., 1992. Geology of Iron-Copper Deposits in EasternHubei Province, China. Metallurgic Industry Press, Beijing, pp. 1–192 (in Chinese).
Simon, G., Kesler, S.E., Essene, E.J., 1997. Phase relation among selenides, sulfides, tellurides, and oxides: II. Application to selenide-bearing ore deposits. Econ. Geol. 92, 468–484.
Stein, H.J., 1988. Genetic traits of climax-type granites and molybdenum mineralization, Colorado Mineral Belt. In: Taylor, R.P., Strong, D.F. (Eds.), Recent Advances in the Geology of Granite-Related Mineral Deposits, Special Volume 39. Canadian Institute of Mining and Metallurgy, pp. 394–401.
Sylvester, P.J., Cabri, L.J., Tubrett, M.N., McMahon, G., Laflamme, J.H.G., Peregoedova, A., 2005. Synthesis and evaluation of a fused pyrrhotite standard reference material for platinum group element and gold analysis by laser ablation–ICPMS. In: Tormanen, T.O., Alapieti, T.T. (Eds.), 10th International Platinum Symposium "Platinum Group Elements — From Genesis to Beneficiation and Environmental Impact", Oulu, Finland, pp. 16–20.
Tarkian, M., Eliopoulos, D.G., Economou-Eliopoulos, M., 1991. Mineralogy of precious metals in the Skouries porphyry copper deposit, northern Greece. Neues Jahrbuch fur Mineralogie Abhand 12, 529–537.
Tarkian, M., Hunken, U., Tokmakchieva, M., Bogdanov, K., 2003. Precious-metal distribution and fluid-inclusion petrography of the Elatsite porphyry copper deposit, Bulgaria. Miner. Deposita 38, 261–281.
Tarkian, M., Stribrny, B., 1999. Platinum-group elements in porphyry copper deposits: a reconnaissance study. Mineral. Petrol. 65, 161–183.
Tian, J., Zhang, Y., Cheng, J.M., Sun, S.Q., Zhao, Y.J., 2019. Short wavelength infra-red (SWIR) characteristics of hydrothermal alteration minerals in skarn deposits: example from the Jiguanzui Cu–Au deposit, Eastern China. Ore Geol. Rev. 106, 134–149.
Voudouris, P., Repstock, A., Spry, P.G., Frenzel, M., Mavrogonatos, C., Keith, M., Tarantola, A., Melfos, V., Tombros, S., Zhai, D., Cook, N.J., Ciobanu, C.L., Schaarschmidt, A., Rieck, B., Kolitsch, U., Falkenberg, J.J., 2022. Physicochemical constraints on indium-, tin-, germanium-, gallium-, gold-, and tellurium-bearing mineralizations in the Pefka and St Philippos polymetallic vein- and breccia-type deposits, Greece. Ore Geol. Rev. 140, 104348.
Wang, M.F., Gutzmer, J., Michalak, P.P., Guo, X.N., Xiao, F., Wang, W., Liu, K., 2014. PGE geochemistry of the Fengshan porphyry–skarn Cu–Mo deposit, Hubei Province, Eastern China. Ore Geol. Rev. 56, 1–12.
Wang, M.F., Zhao, R.Z., Shang, X.Y., Wei, K.T., An, W.W., 2020. Factors controlling Pt–Pd enrichments in intracontinental extensional environment: implications from Tongshankou deposit in the Middle-Lower Yangtze River metallogenic belt, Eastern China. Ore Geol. Rev. 124, 1–13.
Wilkinson, J.J., 2013. Triggers for the formation of porphyry ore deposits in magmatic arcs. Nat. Geosci. 6, 917–925.

Wood, S.A., 1987. Thermodynamic calculations of the volatility of the platinum group elements (PGE): the PGE content of fluids at magmatic temperatures. Geochim. Cosmochim. Acta 51, 3041–3050.

Xie, G.Q., Mao, J.W., Li, R.L., Beirlein, F., 2008. Geochemistry and Nd–Sr isotopic studies of Late Mesozoic granitoids in the southeastern Hubei province, Middle-Lower Yangtze River belt, Eastern China: petrogenesis and tectonic setting. Lithos 104, 216–230.

Xie, G.Q., Mao, J.W., Zhao, H.J., 2011a. Zircon U-Pb geochronological and Hf isotopic constraints on petrogenesis of late Mesozoic intrusions in the southeast Hubei Province, Middle-Lower Yangtze River belt, east China. Lithos 125, 693–710.

Xie, G.Q., Mao, J.W., Zhao, H.J., Duan, C., Yao, L., 2012. Zircon U-Pb and phlogopite 40Ar–39Ar age of the Chengchao and Jinshandian skarn Fe deposits, southeast Hubei Province, Middle-Lower Yangtze River Valley metallogenic belt, China. Miner. Deposita 47, 633–652.

Xie, G.Q., Mao, J.W., Zhao, H.J., Wei, K.T., Jin, S.G., Pan, H.J., Ke, Y.F., 2011b. Timing of skarn deposit formation of the Tonglushan ore district, southeastern Hubei Province, Middle-Lower Yangtze River Valley metallogenic belt and its implications. Ore Geol. Rev. 43, 62–77.

Xie, G.Q., Zhu, Q.Q., Yao, L., Wang, J., Li, W., 2013, Discussion onregional metal mineral deposit model of late Mesozoic Cu-Fe-Au polymetallic deposits in the southeast Hubei province: Bulletin of Mineralogy, Petrology and Geochemistry, v. 32, p. 418–426 (in Chinese with English abs.).

Xie, G.Q., Mao, J.W., Li, W., Zhu, Q.Q., Liu, H.B., Jia, G.H., Li, Y.H., Li, J.J., Zhang, J., 2016. Different proportion of mantle-derived noble gases in the Cu–Fe and Fe skarn deposits: He–Ar isotopic constraint in the Edong district, Eastern China. Ore Geol. Rev. 72, 343–354.

Xie, G.Q., Han, Y.X., Li, X.H., 2019a. A preliminary study of characteristics of dispersed metal-bearing deposits in Middle-Lower Yangtze River Metallogenic Belt. Mineral Resour. Geol. 4, 729–738 in Chinese with English abstract.

Xie, G.Q., Mao, J.W., Richards, J.P., Han, Y.X., Fu, B., 2019b. Distal Au deposits associated with Cu-Au skarn mineralization in the Fengshan Area, eastern China. Econ. Geol. 114, 127–142.

Xiong, Y., Wood, S.A., 2000. Experimental quantification of hydrothermal solubility of platinum-group elements with special reference to porphyry copper environments. Mineral. Petrol. 68, 1–28.

Zhai, D.G., Williams-Jones, A.E., Liu, J.J., Tombros, S.F., Cook, N.J., 2018. Mineralogical, fluid inclusion and multiple isotope (H-O-S-Pb) constraints on the genesis of the Sandaowanzi epithermal Au-Ag-Te deposit, NE China. Econ. Geol. 113, 1359–1382.

Zhai, Y.S., Yao, S.Z., Lin, X.D., Zhou, X.N., Wan, T.F., Jin, F.Q., Zhou, Z.G., 1992. Fe–Cu–Au Metallogeny of the Middle-Lower Changjiang Region. Geological Publishing House, Beijing, pp. 1–235 in Chinese.

Zhang, W., 2015. Ore genesis of the Jiguanzui Cu–Au deposit in Southeastern Hubei Province. China University of Geosciences Press, Wuhan, China, pp. 1–127 in Chinese.

Zhu, Q.Q., Xie, G.Q., Mao, J.W., Hou, K.J., Sun, J.F., Jiang, Z.S., 2017. Formation of the Jinshandian Fe skarn ore feld in the Edong district, eastern China: constraints from U-Pb and 40Ar/39Ar geochronology. Ore Geol. Rev. 86, 1–20.